PLOS CLIMATE

RESEARCH ARTICLE

Atmosphere and ocean energy transport in extreme warming scenarios

Alyssa N. Poletti[1]*, Dargan M. W. Frierson[1], Travis Aerenson[1], Akshaya Nikumbh[2,3], Rachel Carroll[4], William Henshaw[5], Jack Scheff[6]

1 Department of Atmospheric Sciences, University of Washington, Seattle, Washington, United States of America, **2** Geophysical Fluid Dynamics Laboratory (NOAA), Princeton, New Jersey, United States of America, **3** Atmospheric and Oceanic Sciences (AOS), Princeton University, Princeton, New Jersey, United States of America, **4** Collingwood Research, Lincolnville, Maine, United States of America, **5** EarthDefine, Seattle, Washington, United States of America, **6** Department of Geography and Earth Sciences, University of North Carolina at Charlotte, Charlotte, North Carolina, United States of America

* apolet@uw.edu

Citation: Poletti AN, Frierson DMW, Aerenson T, Nikumbh A, Carroll R, Henshaw W, et al. (2024) Atmosphere and ocean energy transport in extreme warming scenarios. PLOS Clim 3(2): e0000343. https://doi.org/10.1371/journal.pclm.0000343

Editor: Ahmed Kenawy, Mansoura University, EGYPT

Received: July 6, 2023

Accepted: December 18, 2023

Published: February 1, 2024

Peer Review History: PLOS recognizes the benefits of transparency in the peer review process; therefore, we enable the publication of all of the content of peer review and author responses alongside final, published articles. The editorial history of this article is available here: https://doi.org/10.1371/journal.pclm.0000343

Data Availability Statement: All data is available for download from the Earth System Grid Federation (ESGF) World Climate Research Programme CMIP6 online database (https://esgf-

Abstract

Extreme scenarios of global warming out to 2300 from the SSP5-8.5 extension scenario are analyzed in three state-of-the-art climate models, including two models with climate sensitivity greater than 4.5˚C. The result is some of the largest warming amounts ever seen in simulations run over the historical record and into the future. The simulations exhibit between 9.3 and 17.5˚C global mean temperature change between pre-Industrial and the end of the 23rd century. The extremely large changes in global temperature allow exploration of fundamental questions in climate dynamics, such as the determination of moisture and energy transports, and their relation to global atmosphere-ocean circulation. Three models performed simulations of SSP5-8.5 to 2300: MRI-ESM2-0, IPSL-CM6A-LR, and CanESM5. We analyze these simulations to improve understanding of climate dynamics, rather than as plausible futures. In the model with the most warming, CanESM5, the moisture content of the planet more than doubles, and the hydrologic cycle increases in intensity. In CanESM5 and IPSL-CM6A-LR nearly all sea ice is eliminated in both summer and winter in both hemispheres. In all three models, the Hadley circulation weakens, the tropopause height rises, and storm tracks shift poleward, to varying degrees. We analyze the moist static energy transports in the simulations using a diffusive framework. The dry static energy flux decreases to compensate for the increased moisture transport; however the compensation is imperfect. The total atmospheric transport increases but not as quickly as expected with a constant diffusivity. The decrease in eddy intensity plays an important role in determining the energy transports, as do the pattern of cloud feedbacks and the strength of ocean circulations.

1. Introduction

CO2 concentrations are higher than in 10 million years [1]. Industry-induced changes to atmospheric compositions have already drastically changed our climate through extreme

node.llnl.gov/search/cmip6/). Cartopy uses BaseMaps from here: https://www.naturalearthdata.com/about/terms-of-use/ which are under Public Domain.

Funding: DWMF and ANP are supported by NSF Award AGS-1665247. The funders had no role in study design, data collection and analysis, decision to publish, or preparation of the manuscript. The authors TA, AN, RC, WH, and JS received no specific funding for this work.

Competing interests: The authors have declared that no competing interests exist.

weather events [2, 3], such as heat extremes [4, 5], severe droughts, and heavy precipitation [6, 7]. Further, the CO2 which has already been emitted will remain in the atmosphere for millennia [8–10]. Long-term consequences of high CO2 concentrations include ice sheet melt and sea level rise, which will continue to increase for many centuries [11], while temperatures stay high and other climate impacts persist [12]. Yet, global climate model (GCM)-based investigations into future climate change typically stop at the end of the 21st century.

CMIP5 (Coupled Model Intercomparison Project Version 5) [13, 14] had the first scenarios with emissions and concentrations extended to 2300, known as the Extended Concentration Pathways (ECPs). The ECPs were used in Chapter 12 of the Working Group 1 contribution to the IPCC 5th Assessment report (AR5) [15], most prominently in a section on climate change beyond 2100. Most of the ECP8.5 experiments analyzed in AR5 were run using Earth-System Models of Intermediate Complexity (EMICs) [16–18] Global-mean temperature and Atlantic Meridional Overturning Circulation (AMOC) at 30˚N were analyzed for the few fully-coupled GCMs as well as the ECPs. Within GCMs, the global temperature increases by 4 to 15 K and the AMOC at 30˚N decreases by a factor of 2 to 6 in RCP8.5 extension experiments in Collins et al. (2014), in 2300 as compared with the pre-Industrial climate [15].

Other work using the high radiative forcing ECPs has highlighted some unique aspects of the very high temperature climates. For studies of sea ice, this includes annually ice-free conditions in the Arctic [19, 20]; and mechanisms of abrupt Arctic winter sea ice loss [21, 22]. Another focus of prior work was the lack of abrupt changes in the AMOC, despite a diversity of changes in strength across models [23].

For the CMIP6 data solicitation the Scenario Model Intercomparison Project (ScenarioMIP) requested fully coupled runs of a new high-emissions scenario called the shared socioeconomic pathway 5 with 8.5 W/m^2 at 2100 (SSP5-8.5) to be simulated to the year 2300 (hereafter referred to as SSP5-85ext) [24]. In Section 4.7.1.2 of the Working Group 1 contribution to the IPCC 6th Assessment Report (AR6), the SSP5-85ext simulations are studied, showing global temperature ranging from 9–17˚C above pre-Industrial, global land precipitation increasing by 0.3–0.6 mm/day, and no September Arctic sea ice [11].

This study examines the SSP5-85ext extreme warming scenario from three different CMIP6 climate models, with simulations integrated until 2300. In particular, we focus on the poleward transport of heat in the much warmer climate and on related variables such as temperature, humidity, precipitation, radiation, and circulation in the atmosphere and ocean. Since water vapor increases rapidly with temperature, we hypothesize large increases in the poleward transport of latent energy within midlatitudes, and equatorward transport within the tropics [25, 26]. Increased latent energy flux may result in weakened equator-to-pole temperature gradients, which would decrease the poleward transport of dry static energy and potentially weaken eddies [27]. Many previous studies have suggested the usefulness of diffusion of moist static energy to understand changes in atmospheric heat transport in different climate regimes [28–33]. Large weakening of eddies would likely imply large decreases in diffusivity, which is not always included in energy balance models.

An additional factor of importance is the response of the ocean circulation to increasing temperature. Since the AMOC plays an important role in determining temperature gradients at a global scale [34, 35], there will likely be interactions among the AMOC, temperature gradients, and dynamics. Wind-driven ocean circulation responds to changes in tropical and midlatitude surface winds associated with processes such as the poleward expansion of the tropics [36], the poleward shift of midlatitude eddies [37], and changes in strength of the Hadley cell [38, 39], among other phenomena.

This paper is organized as follows: Section 2 describes the model simulations used in this study. In Section 3 we begin by showing 1 changes in temperature, humidity and net

precipitation, along with the atmospheric circulation, which helps to explain aspects of the precipitation changes in both the tropics and the extratropics, and 2. an analysis of how the poleward transport of energy changes in the warmed climate, including moist and dry static energy, and ocean heat transport. We additionally examine the role of cloud-radiative effects and midlatitude eddy intensity, arguing that both cloud effects and eddy intensity are important for determining how energy is transported. In Section 4 we further discuss our results and state conclusions.

2. Methods and models

The SSP5 set of scenarios represents intense development across the world, powered by fossil fuels [24]. The SSP5-8.5 scenario in particular reaches very large radiative forcing of approximately 8.5 W/m ^{2} by 2100 (Fig 1A), higher than any other scenario. By 2100 in SSP5-8.5, CO $_2$ concentrations are 1135 ppm, and CO_2 makes up 82% of the radiative forcing in SSP5-8.5 at 2100 (Fig 1) [40]. It is generally thought that the emissions in the RCP8.5 scenario were unrealistically large given the recent trajectory of energy across the world [41], and the SSP5-8.5 scenario is probably similarly unlikely during the 21st century. It should be noted however that all SSP and RCP scenarios (extension or not) are concentration-forced, not emissions-forced. This means that each concentration pathway could be generated with a different emissions pathway, and a larger or smaller than expected carbon cycle response.

In SSP5-8.5ext, emissions ramp downwards from 2100 levels to zero in 2250, for fossil CO_2 and non-CO_2 emissions. Land-use related non-CO $_2$ emissions are held steady at 2100 values, and land use CO $_2$ emissions are ramped up to zero by 2150. The other two extension scenarios in CMIP6, SSP1-2.6 and SSP5-3.4-OS, involve large mitigation efforts, so the SSP5-8.5ext scenario is the only high radiative forcing scenario run past 2100 in ScenarioMIP.

The SSP5-8.5ext scenario in 2300 has 2162 ppm CO_2 (~12.5 W/m ^{2} radiative forcing), 1112 ppb CH $_4$ (0.2 W/m^2 radiative forcing), and 410 ppb N_2O (0.4 W/m^2) (Fig 1A). Land use forcing is -0.2 W/m ^{2} and other forcing agents, including aerosols, F-gases, and tropospheric ozone have absolute value less than 0.1 W/m^2. The total radiative forcing of ~13.0 W/m^2 in 2300 is thus almost exclusively due to CO_2. The ECP8.5 scenario from CMIP5 had a slightly larger total forcing in 2300, with more forcing from methane, and a different time dependence. In this study, we focus on the SSP5-8.5 simulations only.

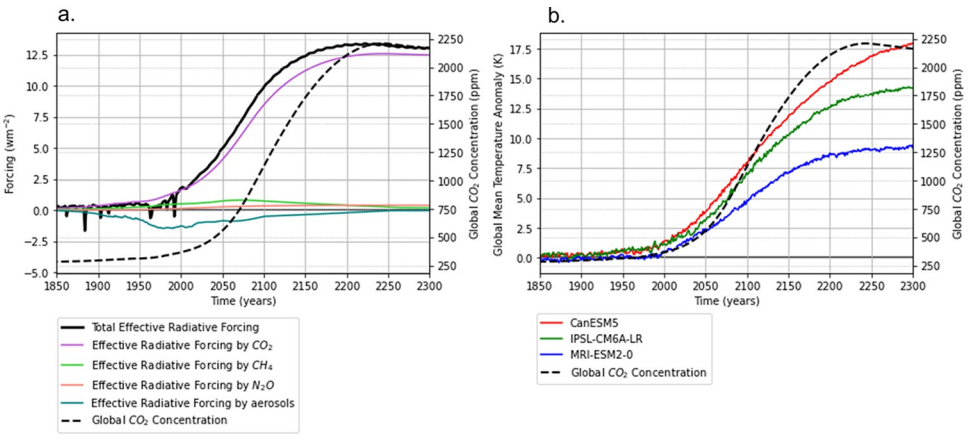

Fig 1. **(A)** The effective radiative forcing of CO2, CH4, N2O, aerosols and in total against time for SSP5-8.5ext simulations (solid) and the global CO2 concentration (dashed) against time for SSP5-8.5ext simulations. **(B)** The global mean temperature anomaly for CanESM5, IPSL-CM6A-LR, and MRI-ESM2-0 (solid) against time for historical (1850–2015) and SSP5-8.5ext (2015–2300), and the global CO2 concentration (dashed) against time for SSP5-8.5ext.

https://doi.org/10.1371/journal.pclm.0000343.g001

There are three models that have run the SSP5-8.5ext simulations: CanESM5, from the Canadian Centre for Climate Modeling and Analysis [42], MRI-ESM2-0 [43], from the Meteorological Research Institute, and IPSL-CM6A-LR [44], from the Institut Pierre-Simon Laplace. Fan et al. (2020) compares an ensemble of 16 GCMs to three periods of observed historical warming trends (˚C/decade) from 1901 to 2014 [45]. This analysis found that CanESM5 and IPSL-CM6A-LR overestimate warming trends from 1941 to 2014, which could indicate an overly large sensitivity to radiative forcing in these two models. MRI-ESM2-0 underestimates warming trends from 1941 to 1970 and overestimates warming trends from 1971 to 2014. All three models approximately reproduce historical warming trends from 1901 to 1940. Much of our analysis consists of comparison among three climate states. The first time period is the simulated pre-Industrial climate (piControl), where the atmospheric constituents are set to 1850 levels. We average over the final 100 years of the piControl simulation to avoid simulation drift during earlier portions while the model is equilibrating. The second time period is the average of the years 2076–2100 in the SSP5-8.5 simulations, henceforth referred to as the "intermediate period," and the third time period is from 2276–2300 of the SSP5-8.5ext, which we call the "hot period." The intermediate period of SSP5-8.5 has been widely studied both in comparison with the piControl climate, and with the other members of the ScenarioMIP suite of simulations [46, 47], hence the intermediate period is a useful comparison point for the "hot period," which experiences extreme warming.

3. Results

3.1 Basic climatological fields

a. Surface temperature. Global averaged 2-meter surface air temperature change is plotted for each model in Fig 1B. The globally-averaged temperature change in these three models in the intermediate and hot period, as well as the percentage of total warming that occurs by the intermediate period is shown in Table 1 and Fig 1B. Roughly half of the total warming occurs by the intermediate period, and models with more warming experience a smaller fractional change pre-2100.

The equilibrium climate sensitivities to doubling CO_2 of CanESM5, IPSL-CM6A-LR, and MRI-ESM2-0, calculated using the method derived by Gregory et al. (2004) [48], and compiled for CMIP6 by Meehl et al. (2020) [49], are 5.6˚C, 4.6˚C, and 3.2˚C, respectively. The transient climate responses for CanESM5, IPSL-CM6A-LR, and MRI-ESM2-0 are 2.8˚C [42], 1.96˚C [44], and 1.64˚C [49], respectively. The ratio between the hot period anomalous temperature change and the equilibrium climate sensitivity are close to 3 for each model; the TCR has a less consistent relationship with the hot period warming, which is expected since the models have been at a stable forcing for more than a century by the end of the run (Fig 1A). The ratio of radiative forcing in the hot period (13.0 W/m^2) to the forcing of doubling CO_2 (3.7 W/m^2) is 3.5, which suggests that the hot period warming is slightly less than would be expected from a linear, equilibrium response to the radiative forcing. From Fig 1B, it is clear that all three models are still warming in 2300, despite the near-constant forcing over the previous century.

Table 1. Global averaged temperature anomaly in the intermediate period, hot period, and the percentage of warming that has occurred by the intermediate period.

Global Mean Temperature Anomaly			
Model	**Intermediate Period (K)**	**Hot Period (K)**	**Percentage (%)**
CanESM5	8.13	17.5	46.5
IPSL-CM6A-LR	7.10	14.0	50.7
MRI-ESM2-0	4.95	9.3	53.2

https://doi.org/10.1371/journal.pclm.0000343.t001

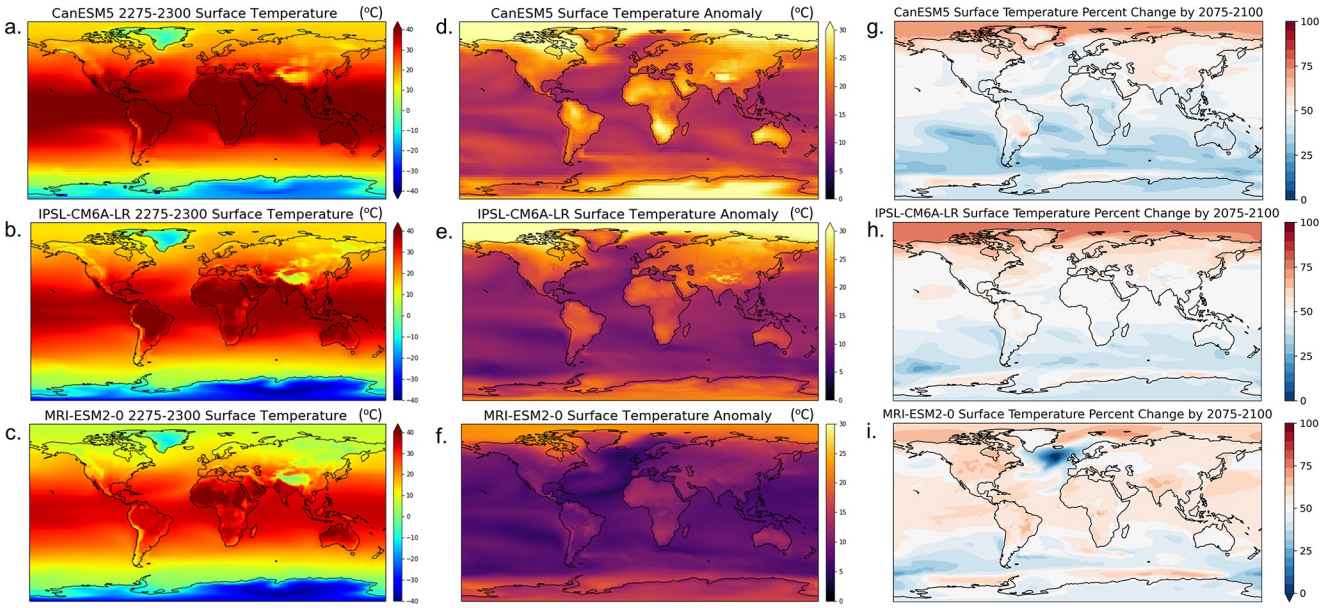

Fig 2. **(A, B, C)** Near-surface temperature averaged over the hot period, **(D, E, F)** the hot period temperature anomalies relative to pre-Industrial, and **(G, H, I)** the percent change in surface temperature by the intermediate period, calculated as the ratio of the intermediate period temperature anomalies divided by the hot period temperature anomalies relative to pre-Industrial. These maps were made using the Cartopy Robinson projection. (https://scitools.org.uk/cartopy/docs/v0.15/crs/projections.html) which uses data from Natural Earth (https://www.naturalearthdata.com/downloads/110m-physical-vectors/).

https://doi.org/10.1371/journal.pclm.0000343.g002

The 2-meter surface air temperatures averaged over the hot period are shown in Fig 2 alongside their anomalies from pre-Industrial and the percentage of the total change that occurs during the simulation happens during the 21st century,

$$Percentage = \Delta T(intermediate)/\Delta T(hot)*100\%.$$

In the right-hand column of Fig 2, blue coloration indicates regions where there is more warming between the intermediate period and the hot period than occurs between the pre-Industrial and intermediate periods (and vice-versa for red coloration). The plots are presented in descending order of climate sensitivity: CanESM5, IPSL-CM6A-LR, and MRI-ESM2-0. In each model there are regions where the annual mean temperature over tropical continents exceeds 40˚C in the hot period, and in CanESM5, nearly the entire tropics exceeds 40˚C in the annual mean. In CanESM5, tropical warming happens more between the intermediate period and the hot period, as indicated by the blue colors in Fig 2G. In IPSL-CM6A-LR, tropical heating occurs approximately equally before and after 2100 (Fig 2H). Whereas, in MRI-ESM2-0, tropical heating occurs primarily before the intermediate period, as shown by the red coloring in Fig 2I. In the hot period in CanESM5 and IPSL-CM6A-LR, the 0˚C annual average contour only exists over Antarctic and Greenland ice sheets (the topography of which is prescribed). MRI-ESM2-0 also has a small region below freezing in the Himalayas.

The middle column of Fig 2 shows the temperature anomaly during the hot period, compared to the piControl climatology. The changes are greatest for each model in the Arctic, which is consistent with the polar amplification that has been widely studied [50–52]. In CanESM5 and IPSL-CM6A-LR the Arctic warming exceeds 30˚C, and in MRI-ESM2-0 it gets as high as 25˚C. In each model the average warming north of 60˚ N is 26.5˚C, 23.7˚C, and

16.2˚C for CanESM5, IPSL-CM6A-LR, and MRI-ESM2-0 respectively. The Arctic warming of each model is between a factor of 1.5 and 1.75 greater than the global average, with MRI-ESM2-0 having the strongest Arctic amplification ratio of 1.74, then IPSL-CM6A-LR with 1.69, and CanESM5 has the lowest amplification ratio of 1.51. In each model, more than half of the Arctic warming occurs by 2100 (Fig 2G–2I). Namely, the impact of Arctic amplification is most prominent before 2100, likely due to substantial sea ice loss by 2100 [50–52]. Ono et al. (2022) showed that the rate of sea-ice loss with increasing temperature is non-monotonic in SSP5-8.5 because once the sea-ice extent is sufficiently small, the loss rate is lower than occurs in a cooler climate (even with greater amounts of warming) [53].

Outside of the Arctic, the greatest warming is seen over subtropical land areas, with temperature changes that are often 50% higher than the global average warming in each model. CanESM5 shows particularly large warming over Southern Africa, Australia, and equatorial South America, with temperature changes that are 70% larger than the global mean. Equatorial South America has a rather different temperature change across the three models. There is variability across these models regarding when land warming occurs. In CanESM5, the pronounced warming over Southern Africa and Australia occurs primarily between the intermediate and hot periods. In IPSL-CM6A-LR, the warming over Southern Africa, Australia, and equatorial South America occurs nearly equally before and after the intermediate period. Finally, in MRI-ESM2-0, warming over those three regions occurs primarily before the intermediate period.

b. Surface humidity. Fig 3 shows the surface specific humidity anomalies for the hot period and the percentage of the total change that occurs by the intermediate period. The

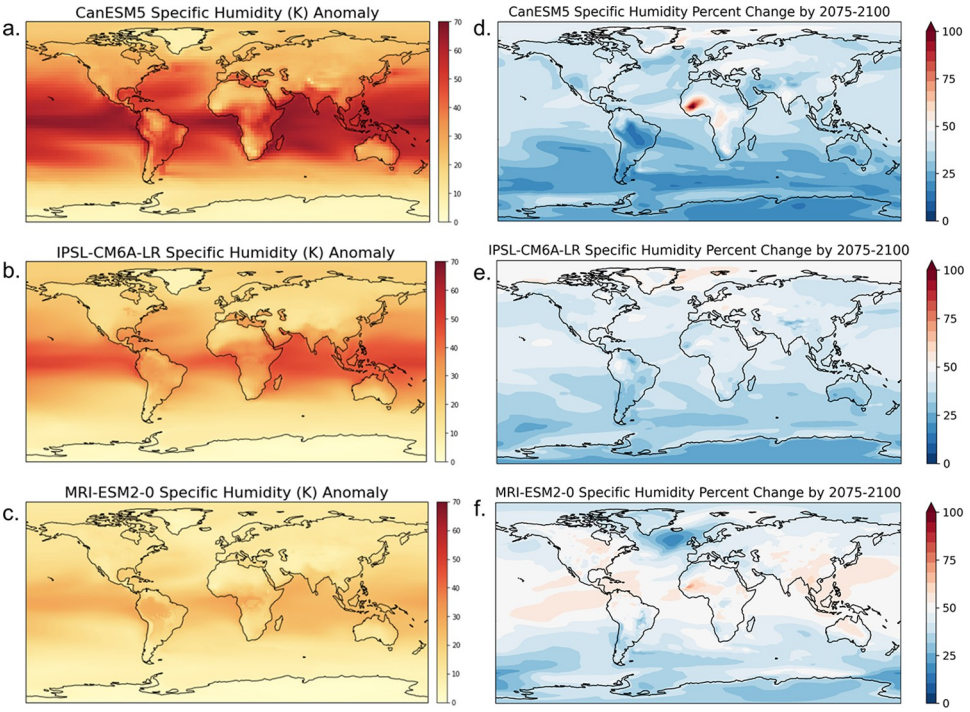

Fig 3. **(A, B, C)** Anomalies of surface specific humidity relative to pre-Industrial, and **(D, E, F)** the percent change from the intermediate period to the hot period, calculated as the ratio of the surface specific humidity anomaly in the intermediate period and the anomaly in the hot period. These maps were made using the Cartopy Robinson projection (https://scitools.org.uk/cartopy/docs/v0.15/crs/projections.html) which uses data from Natural Earth (https://www.naturalearthdata.com/downloads/110m-physical-vectors/).

https://doi.org/10.1371/journal.pclm.0000343.g003

specific humidity is shown in units of Kelvin (which is converted by multiplying by the ratio of latent heat of vaporization of water and the specific heat at constant pressure of air). This convention has greater utility for use in interpreting moist static energy (MSE) which we examine later in the paper.

The tropical specific humidity more than doubles in CanESM5 and IPSL-CM6A-LR and increases by a factor of 1.6 in MRI-ESM2-0. In CanESM5 and IPSL-CM6A-LR, globally the majority of specific humidity changes occur after 2100 (Fig 3D–3F), in part due to nonlinearity in the Clausius-Clapeyron relation. Exceptions to this include the Atlantic Ocean east of Greenland in CanESM5 and IPSL-CM6A-LR, parts of west and central Africa in CanESM5, and parts of the tropics and Northern Hemisphere (NH) land in MRI-ESM2-0, in which there are larger changes in the intermediate period.

In all three models, the spatial pattern of the percentage change in specific humidity that occurs prior to 2100 is similar in structure to that of surface temperature in regions outside of the Arctic. In CanESM5 and IPSL-CM6A-LR, the Southern Hemisphere sees more warming in the hot period than the intermediate period (blue coloration in Fig 2G–2I), which contributes to larger increases in specific humidity in the Southern Hemisphere in the hot period. While the Arctic warms more in the intermediate period than the hot period (red coloration in Fig 2G–2I), the specific humidity changes occur mostly in the hot period (in CanESM5) or equally in either period (IPSL-CM6A-LR); this is due to the nonlinearity of the Clausius-Clapeyron equation under the very large Arctic temperature changes.

Fig 4 shows the relative humidity anomalies of the hot period and intermediate periods relative humidity anomalies from pre-Industrial for the hot period, the intermediate periods, and as well as the difference between the hot and intermediate period. The surface relative humidity change is characterized by small increases over most ocean areas in each model (Fig 4). Exceptions to this are in the Arctic, where relative humidity decreases in each model.

The relative humidity changes above land masses are very different from model to model. The IPSL-CM6A-LR model shows substantial drying over nearly all continental regions by 2300. This drying occurs primarily before the intermediate period, especially in the Arctic and the Amazon. CanESM5 has even larger relative humidity changes over some land locations like the Amazon and the Congo Rainforest but has increasing humidity over Arctic and some tropical locations. The drying in the Amazon occurs primarily before the intermediate period, while the majority of drying in the Congo Rainforest occurs after 2100. The relative humidity change in the MRI-ESM2-0 model is qualitatively similar to that of CanESM5 with significantly less amplitude change. It is expected that global warming causes declines in relative humidity over land [12, 54–56]. Specific humidity over land tends to increase proportionately to specific humidity over ocean; thus, the percent increase in specific humidity with climate change is controlled by ocean warming, which is smaller than land warming [54, 55].

Fig 5 displays the zonal mean of specific and relative humidity, comparing the hot period to pre-Industrial. Specific humidity in the Arctic increases by a much larger fraction than in the tropics. In latitudes greater than 60˚ N, average moisture increases by factors of 5.1, 4.4, and 2.9 for CanESM5, IPSL-CM6A-LR, and MRI-ESM2-0 respectively. The large increase in Arctic moisture content can be explained by the large Arctic warming observed in all three models, since the relative humidity in Figs 4 and 5 show a slight decrease.

c. Precipitation. Precipitation minus evaporation (net precipitation) patterns are shown in Fig 6. The three columns display net precipitation anomalies for the hot period from pre-Industrial, the intermediate period from pre-Industrial, and the hot period from the intermediate period (left to right). Precipitation changes are characterized by a wet-get-wetter pattern that is familiar in global warming scenarios, in which precipitation increases in ascent regions such as the deep tropics, and along the Kuroshio, Gulf Stream, and decreases in subtropical

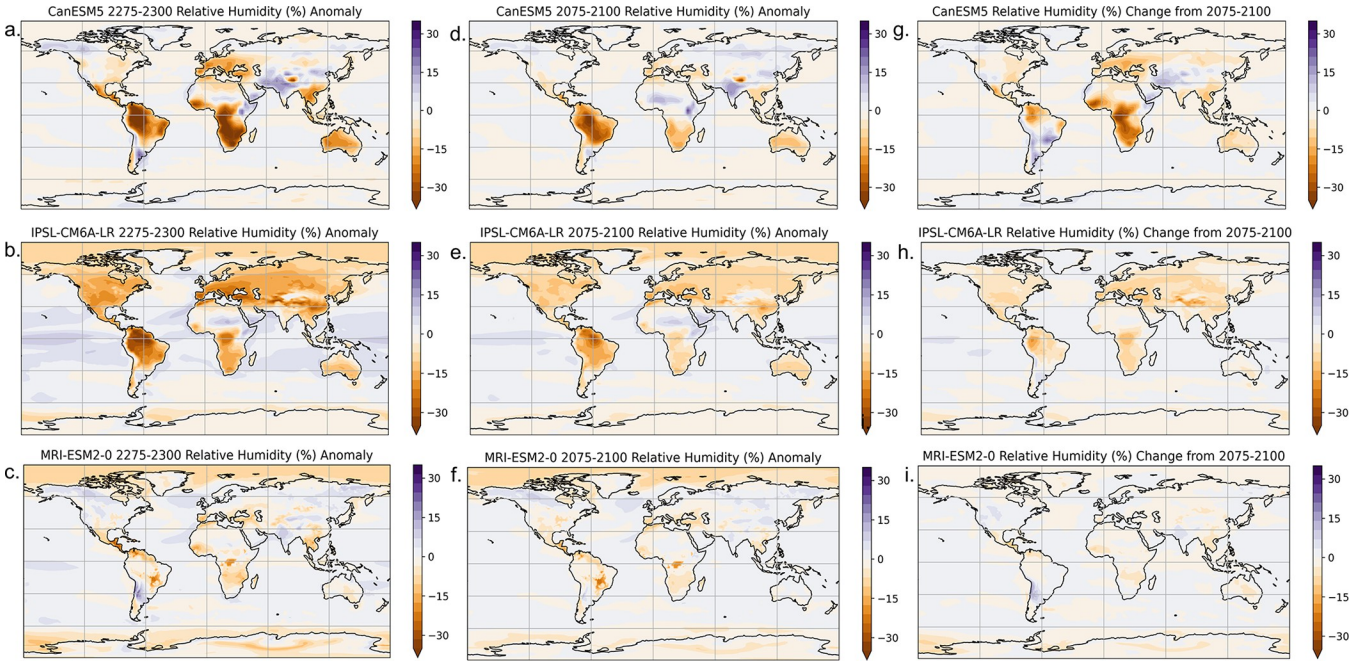

Fig 4. **(A, B, C)** Anomalies of surface relative humidity in the hot period relative pre-Industrial, **(D, E, F)** anomalies of surface specific humidity in the intermediate relative pre-Industrial, and **(G, H, I)** the relative humidity change from 2075–2100, calculated as the hot period relative humidity minus the intermediate period relative humidity. These maps were made using the Cartopy Robinson projection (https://scitools.org.uk/cartopy/docs/v0.15/crs/projections.html) which uses data from Natural Earth (https://www.naturalearthdata.com/downloads/110m-physical-vectors/).

https://doi.org/10.1371/journal.pclm.0000343.g004

descent regions [26]. Nearly all locations in the polar regions of both hemispheres show increases in precipitation. Many subtropical areas experience drying, as do locations on the equatorward edge of the midlatitude storm track, which is in line with the multi-model-mean precipitation patterns taken during the first century of the ScenarioMIP runs [45]. Poleward shifts of circulation, which are analyzed in the next subsection, in part determine the subtropical drying.

Drying in sub-Saharan Africa occurs preferentially between the intermediate and hot periods for all models (Fig 6). In particular, the drying in tropical Africa between the intermediate and hot periods suggests that the more familiar CMIP wetting response in this region (e.g. between the pre-Industrial and intermediate periods in Fig 6) is not fundamental, corroborating the general lack of confidence in this wetting [57, 58].

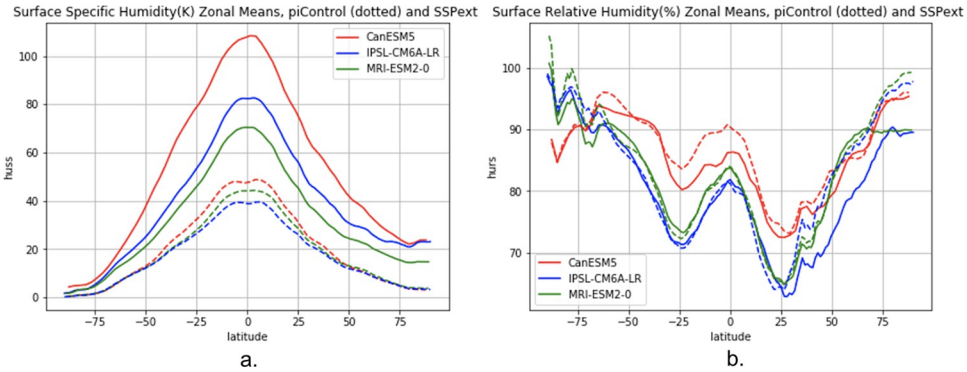

Fig 5. **(A)** The specific and **(B)** relative humidity zonal means, for the hot period (solid) and pre-Industrial (dashed).

https://doi.org/10.1371/journal.pclm.0000343.g005

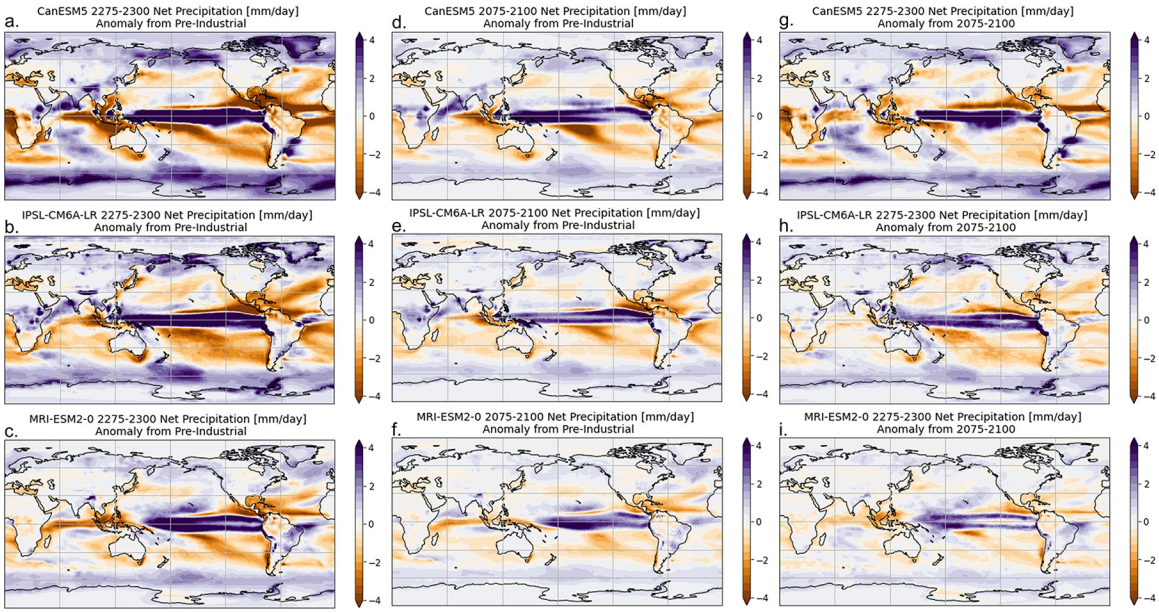

Fig 6. **(A, B, C)** The net precipitation (precipitation minus evaporation) anomaly for the hot period from pre-Industrial, **(D, E, F)** the intermediate period from pre-Industrial, and **(G, H, I)** the hot period anomaly from intermediate period anomaly. These maps are centered at 180 degrees longitudinally so as to better see the ITCZ. These maps were made using the Cartopy Robinson projection (https://scitools.org.uk/cartopy/docs/v0.15/crs/projections.html) which uses data from Natural Earth (https://www.naturalearthdata.com/downloads/110m-physical-vectors/).

https://doi.org/10.1371/journal.pclm.0000343.g006

There are several areas with significant model-to-model differences in the pattern of precipitation. Equatorial Africa moistens in IPSL-CM6A-LR while it dries or exhibits more complex patterns in the other two. These precipitation changes over land explain some of the differences in the surface relative humidity changes. The Atlantic Inter-Tropical Convergence Zone (ITCZ) also exhibits a southward shift in the MRI-ESM2-0 model. While the magnitude of net precipitation changes are roughly equal before and after the intermediate period, changes near the ITCZ occur differently across the models. In CanESM5, north of the Pacific ITCZ has a positive net precipitation anomaly in the intermediate period, but a negative anomaly between the intermediate period and the hot period. Similar areas of drying north of the ITCZ in the later period can be seen in the other two models as well.

d. Atmospheric circulation. The zonally-averaged streamfunction in pre-Industrial (black contours) and the hot period anomaly from pre-Industrial (colors) is plotted in Fig 7A–7C. The zonally-averaged streamfunction at 500hPa for the pre-Industrial (dotted), the intermediate period (dashed), and the hot period (solid) is plotted in Fig 8. The change in the zonally-averaged streamfunction has a complex structure, due to distinct physical processes occurring at different heights and latitudes. In each of the three models, there are streamfunction changes associated with the increase in tropopause height [59], the weakening of the Hadley cells [39], and the widening of the Hadley cells [60].

The increased depth of the Hadley cells can be identified by the positive anomaly above the NH Hadley cell, and the negative anomaly above the Southern Hemisphere (SH) Hadley cell (these anomalies occur between approximately 300 and 100 hPa and between 30S and 30N; Fig 7A–7C). The maximum Hadley circulation strength in the hot period is 55%, 57%, and 85% in the NH compared to the maximum in pre-Industrial, and 73%, 84% and 82% in the SH compared to pre-Industrial, in CanESM5, IPSL-CM6A-LR, and MRI-ESM2-0, respectively. However, the changes to the NH and SH Hadley cells occur at different times.

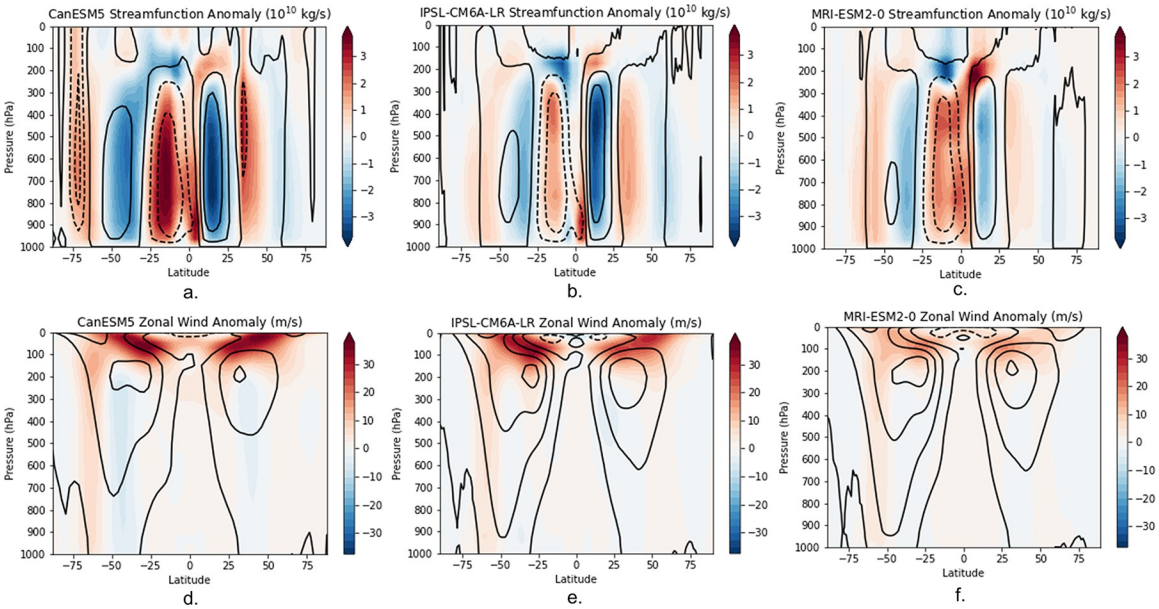

Fig 7. The color contours represent **(A, B, C)** the streamfunction anomaly (10^{10} kg/s) and **(D, E, F)** the zonal wind anomaly (m/s) of CanESM5, IPSL-CM6A-LR, and MRI-ESM2-0. The black contours represent the pre-Industrial. The pre-Industrial streamfunction ranges from -9 to 9x10^{10} kg/s with a contour interval of 3x10^{10} kg/s. The pre-Industrial zonal wind ranges from 0 to 30 m/s with a contour interval of 6 m/s.

https://doi.org/10.1371/journal.pclm.0000343.g007

The decrease in SH Hadley cell (and the SH Ferrel cell) strength occurs predominantly between the intermediate and hot period for all models, while the decrease in the NH Hadley cells occurs both before and after the intermediate period (Fig 8).

We measure the Hadley cell width as the boundary between the Hadley and Ferrel cells at 500 hPa, which is calculated as the latitude at which the 500 hPa meridional streamfunction crosses zero for the first time between the equator and the pole. Time series of the Hadley cell

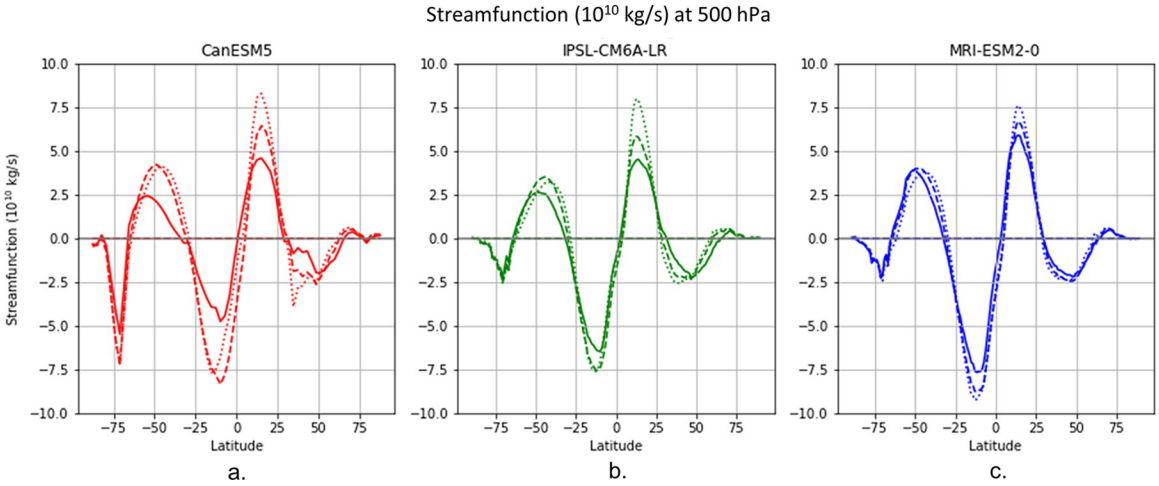

Fig 8. The streamfunction (10^{10} kg/s) at 500hPa for CanESM5 (**A**, red), IPSL-CM6A (**B**, green) and MRI-ESM2-0 (**C**, blue). The solid lines represent the hot period, the dashed lines represent the intermediate period, and the dotted lines represent the pre-Industrial period.

https://doi.org/10.1371/journal.pclm.0000343.g008

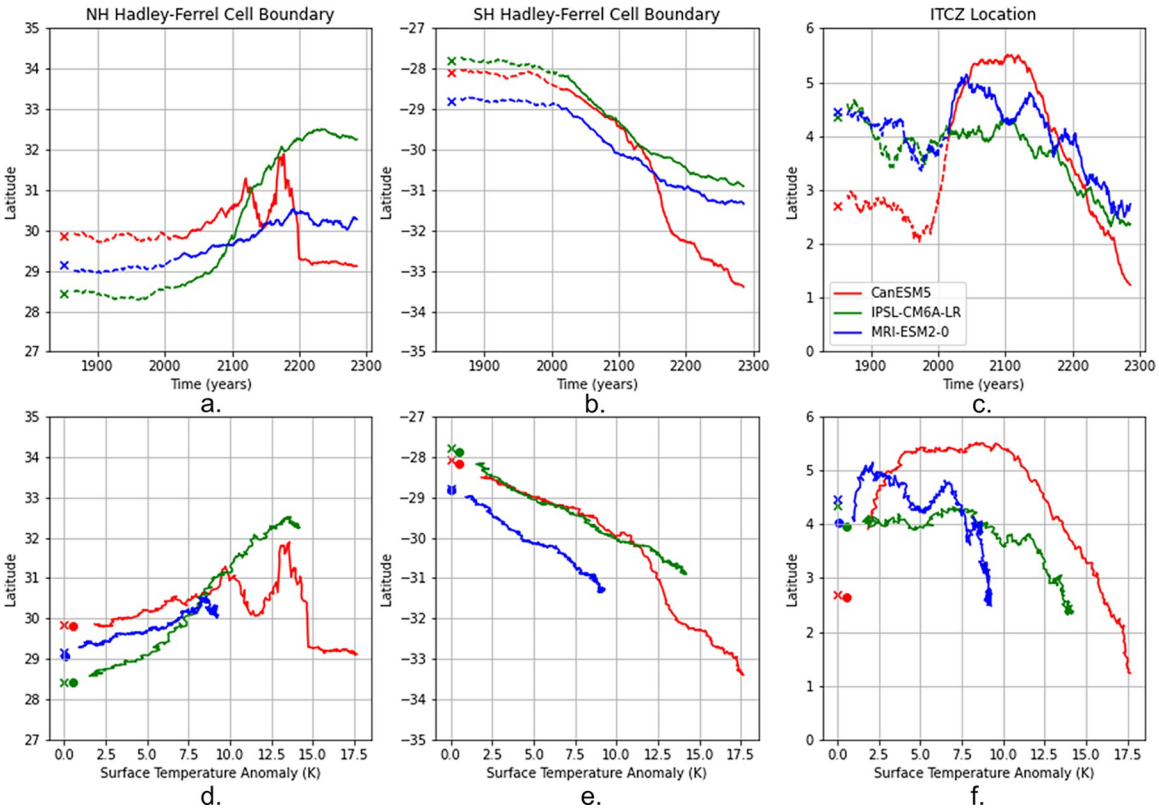

Fig 9. **(A, B, C)** The 30-year running mean NH and SH Hadley-Ferrel Boundary location and ITCZ location versus time, and **(D, E, F)** global mean temperature anomaly from 1850 to 2300. The time and zonally averaged pre-Industrial values are denoted by an X. In the time series figures (top row), the historical data (1850–2015) are denoted by the dashed lines, while the SSP-Ext runs (2015–2300) are denoted by the solid lines. In the temperature anomaly figures (bottom row), the time-mean historical data is denoted by a circle.

https://doi.org/10.1371/journal.pclm.0000343.g009

boundaries in the NH and SH are shown in Fig 9, both as a function of year and of global temperature change. The SH tropical expansion is as large as 5.4 degrees in the CanESM5 model, and is relatively similar as a function of global warming across the three models (Fig 9). The NH Hadley Cell extent, on the other hand, shows significant variability across models, and even within a single time series. In CanESM5, the NH Hadley cell extent vacillates between the years 2100 and 2200 (Fig 9), before contracting to below pre-Industrial values. From Fig 8, it is clear that the zero crossing of the streamfunction in CanESM5 is less well-determined in the hot period, in that there is a range of latitudes near 30 degrees that are close to zero streamfunction. This ambiguity in the Hadley Cell's northern extent in CanESM5 may be a factor in the variability in the NH Hadley Cell boundary after 2100 in Fig 9. Other studies have proposed possible mechanisms for an insignificant NH Hadley cell width change, including enhanced equatorial warming reversing seasonal Hadley Cell expansion [61], dynamic processes due to sea ice loss and ocean heat transport [62], or a large change in natural variability [63]. A more detailed analysis of the large-scale circulation in CanESM5 and other extreme warming scenarios is required to fully understand the mechanisms involved in NH Hadley Cell contraction.

IPSL-CM6A-LR, by contrast, exhibits large NH tropical widening, even more than its SH tropical widening (in final extent and in rate of expansion; Tables 2 and 3). The larger SH Hadley Cell expansion in CanESM5 and MRI-ESM2-0 (when compared to the NH) is consistent with previous literature [64].

Table 2. Latitudinal change in the Hadley-Ferrel Boundary, Ferrel Cell Boundary, ITCZ, and jetstream location in degrees per century. The first value is for the NH and the second value is for the SH (except for the ITCZ which has one location in the NH). The Hadley-Ferrel and ITCZ locations were found by interpolating for subgrid zeros in the 500hPa streamfunction. The outer Ferrel Cell boundary was found by interpolating for subgrid zeros in the zonally averaged zonal wind. The stormtrack was found by interpolating for subgrid zeros in the numerical derivative of surface zonal wind with respect to latitude. Values which do not have a p-value less than 0.05 are italicized. All of the regressions are done on yearly averages.

	Hadley-Ferrel Boundary	Polar- Ferrel Boundary	ITCZ	Stormtrack
CanESM5	*-0.14 ± 0.08* / -2.0 ± 0.05	1.6 ± 0.1 / -0.71 ± 0.02	-1.6 ± 0.07	3.0 ± 0.16 / -2.6 ± 0.05
IPSL-CM6A-LR	1.7 ± 0.05 / -1.0 ± 0.03	2.9 ± 0.5 / -0.55 ± 0.04	-0.77 ±0.07	3.1 ± 0.20 / -1.3 ± 0.06
MRI-ESM2-0	0.37 ± 0.05 / -0.90 ± 0.03	0.87 ± 0.19 / -0.38 ± 0.13	-0.87 ± 0.11	*0.16 ± 0.08* / -0.78 ± 0.06

https://doi.org/10.1371/journal.pclm.0000343.t002

Time series of the Ferrel Cell boundary in the NH and SH as well as the SH stormtrack latitude are shown in Fig 10, both as a function of year and of global temperature change. The boundary between the Ferrel Cell and the Polar Cell also expands with warming in each model (Fig 10). In every model there is greater expansion of the NH Ferrel Cell than the NH Hadley cell, which is especially pertinent in CanESM5, where the NH Hadley cell boundary shrinks equatorward, while the NH Ferrel cell boundary expands poleward. The absolute location of the SH Polar-Ferrel boundary, however, is always at higher latitude than the NH boundary; however, both the SH and NH Polar-Ferrel boundaries approach a limit in their poleward extent. Barnes & Hartmann (2012) postulate that there is a poleward limit to cyclonic wave breaking in midlatitude jets and that the SH jets have already reached this extent [65]. This is consistent with the lesser poleward motion we see in the SH Polar-Ferrel boundary compared to that in the NH.

The bottom row of Fig 7D–7F shows the zonally averaged zonal wind anomalies. The jet stream, defined by the maximum in zonal wind, rises along with the tropopause, decreasing in pressure by 50 to 100 hPa, with a larger rise in the models that warm more. Changes in zonal wind below the tropopause are on the order of several m/s, representing large fractional changes in wind strength especially near the surface. The large poleward shift of the SH jet streams are consistent with the time series of the SH stormtrack, measured as the maximum surface zonal wind, which shows a decrease in latitude between approximately 3.0 and 7.5 degrees (Fig 10).

All three models produce an equatorward shift of the ITCZ in the warm period. Based on surface wind convergence in the piControl runs, the ITCZ is at 2.8–4.5˚ N. By 2300, the convergence shifts to approximately 1.2–2.6˚ N. The vast majority of the equatorward shift of the ITCZ occurs after 2100, especially in CanESM5 where the ITCZ shifts more than 3 degrees northward by 2100 and 4 degrees southward after. The changes in ITCZ location are consistent with the changes in tropical precipitation seen in Fig 6 and described above.

3.2 Poleward energy transports

a. Latent energy, DSE, and MSE transport. The northward transport of latent energy is plotted for both pre-Industrial control and the end of SSP5-8.5ext in Fig 11A. Since the

Table 3. Latitudinal change in the Hadley-Ferrel Boundary, Ferrel Cell Boundary, ITCZ, and jetstream location against global mean temperature anomaly (degrees/K). The first value is for the NH and the second value is for the SH (except for the ITCZ which has one location in the NH). See Table 2 for methods. All values included have a p-value of less than 0.05. All of the regressions are done on yearly averages.

	Hadley-Ferrel Boundary	Polar-Ferrel Boundary	ITCZ	Stormtrack
CanESM5	*-0.01 ± 0.01* / -0.32 ± 0.01	0.27 ± 0.02 / -0.12 ±0.003	-0.23 ± 0.01	0.50 ± 0.02 / -0.41 ± 0.01
IPSL-CM6A-LR	0.34 ± 0.01 / -0.20 ± 0.01	0.58 ± 0.03 / -0.11 ± 0.01	-0.14 ± 0.01	0.63 ± 0.04 / -0.26 ± 0.01
MRI-ESM2-0	0.12 ± 0.01 / -0.27 ± 0.01	0.29 ± 0.06 / -0.11 ± 0.04	-0.24 ± 0.04	0.05 ± 0.02 / -0.23 ± 0.02

https://doi.org/10.1371/journal.pclm.0000343.t003

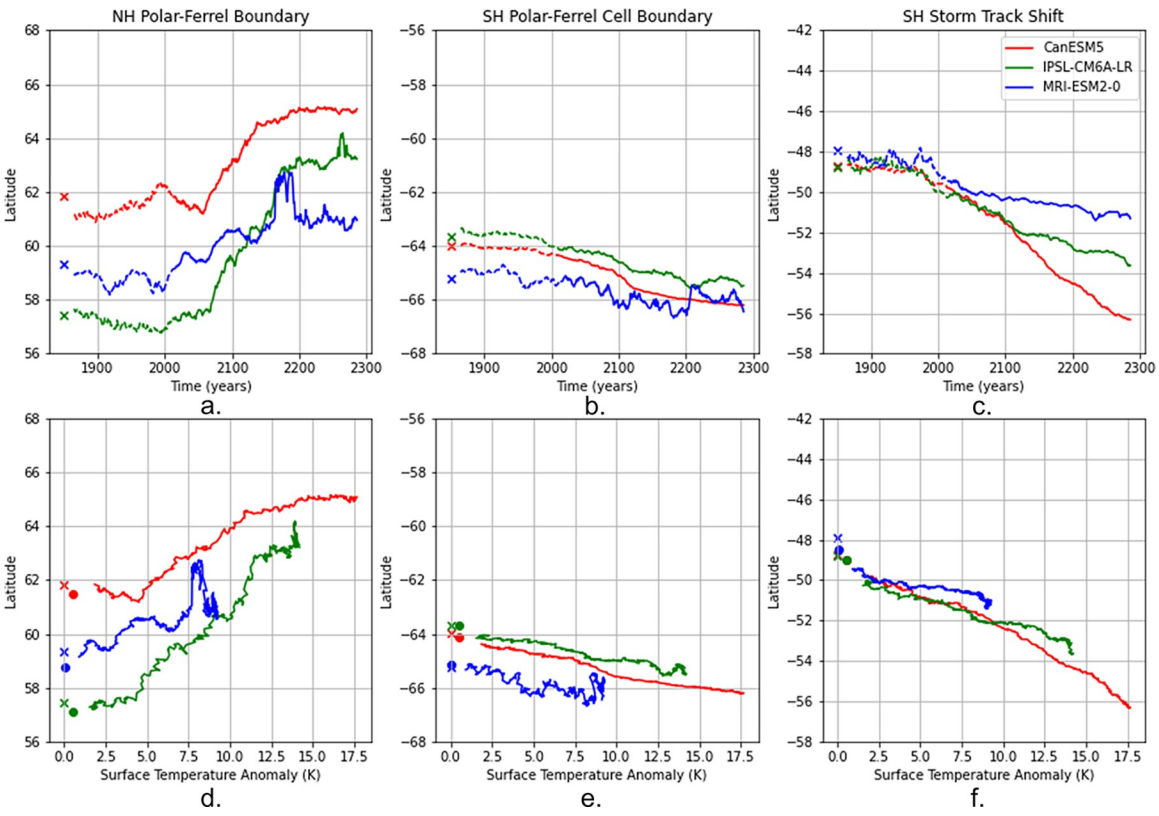

Fig 10. The 30-year running mean of **(A, D)** the NH Polar-Ferrel Cell boundary, **(B, E)** the SH Polar-Ferrel Cell boundary **(C, F)** and the SH storm track location versus time (top row), and versus the global mean temperature anomaly (bottom row) from 1850 to 2300. The time and zonally averaged pre-Industrial values are denoted by an X. In the time series figures (top row), the historical data (1850–2015) are denoted by the dashed lines, while the SSP-Ext runs (2015–2300) are denoted by the solid lines. In the temperature anomaly figures (bottom row), the time and time-mean historical data is denoted by a circle. The piControl stormtrack latitudes for CanESM5, IPSL-CM6A-LR, and MRI-ESM2-0 are 48.7S, 48.8S, and 47.9S respectively.

https://doi.org/10.1371/journal.pclm.0000343.g010

moisture content increases by such a large amount with warming, it is not surprising that the latent energy transport also amplifies quite a bit. In the SH extratropics, for instance, the maximum southward flux increases from less than 3 PW to over 4 PW in each model, with larger increases in models with more temperature change.

The CanESM5 model has a 3 PW increase in southward latent energy transport at 55˚ S (Fig 12A). In the NH extratropics, the maximum northward latent heat transport increases by 1–1.8 PW, depending on the model. At 45˚ N, poleward of its initial extratropical maximum, the northward latent energy flux in the CanESM5 model increases by 2 PW. In both the NH and SH extratropics, the latent heat transport increases more on the poleward side of the maximum than the equatorward side. The latitude of maximum poleward flux shifts poleward in both hemispheres in each model, and the fractional increase in flux reaches a factor of 3–4 in regions poleward of the flux maximum, as compared with 40–100% increase of the maximum value itself. These moisture transport changes are consistent with the large increases in precipitation at high latitudes in each model.

The equatorward latent energy transport within the tropics in the pre-Industrial control is driven by the Hadley circulation. Despite large increases in humidity in the deep tropics, the equatorward transport in the NH tropics does not increase much, meaning the decrease in Hadley cell strength (Fig 7) nearly compensates. The SH tropical transport increases more,

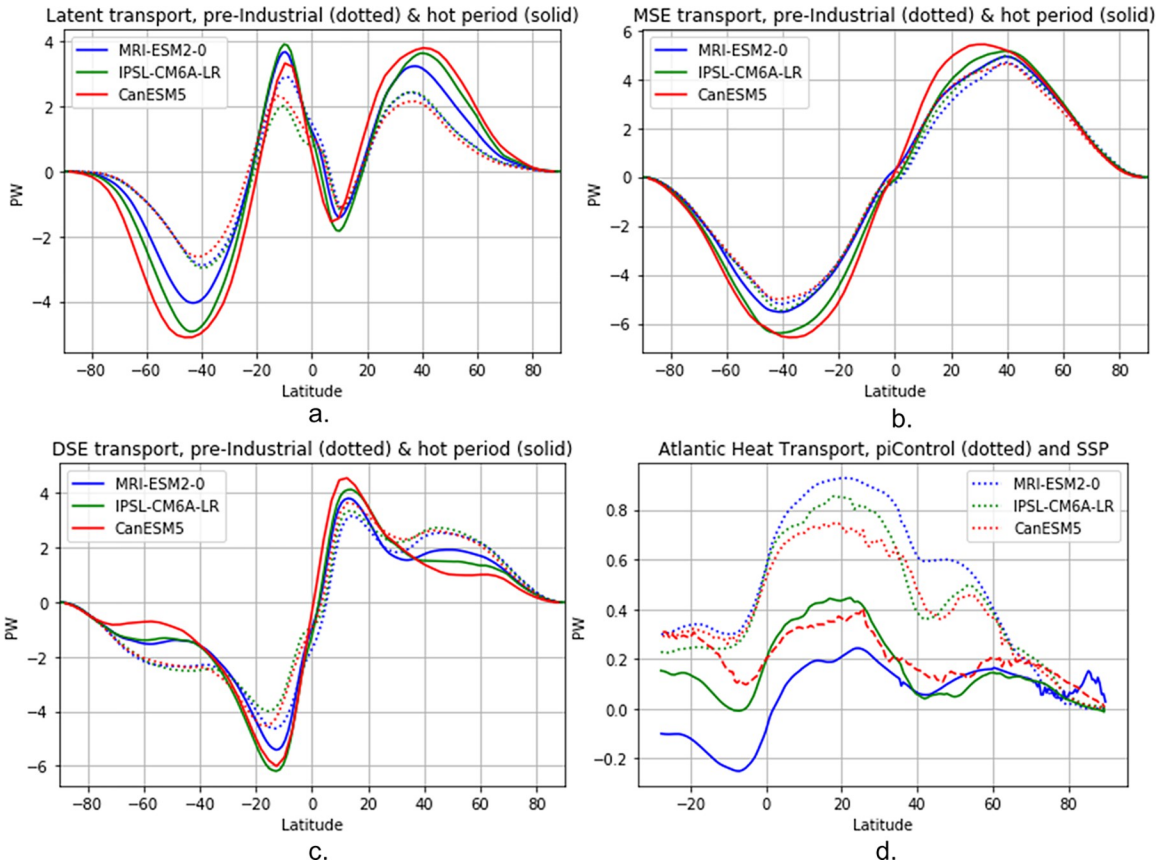

Fig 11. Northward transport of energy from **(A)** latent, **(B)** moist static energy, and **(C)** dry static energy and **(D)** the Atlantic Ocean. Pre-Industrial transports are dotted and hot period transports are solid. The CanESM5 ocean heat transport data for the hot period is averaged between 2156 and 2180, due to data availability, so it is denoted with a dashed line to indicate the different averaging period.

https://doi.org/10.1371/journal.pclm.0000343.g011

especially in the IPSL-CM6A-LR model, but the reduction in Hadley circulation strength also reduces the magnitude of the equatorward moisture flux change.

The northward transport of MSE is plotted in Fig 11B, and its change in Fig 12B. The structure of the transport is similar in pre-Industrial and warmed climate, with poleward transport

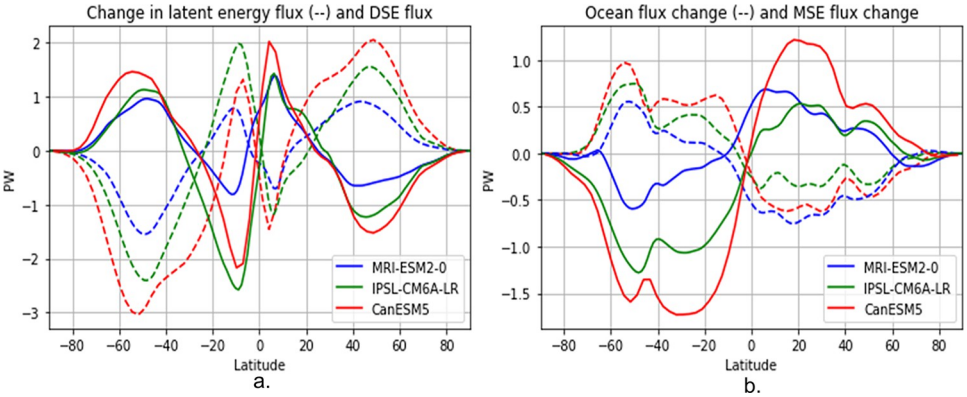

Fig 12. Change in northward transport of energy (hot period minus pre-Industrial) from **(A)** latent (dashed) and DSE (solid), as well as from **(B)** ocean transport (dashed) and MSE (solid).

https://doi.org/10.1371/journal.pclm.0000343.g012

in both hemispheres. The poleward transport increases in all models, but with varying magnitudes. The increase in poleward flux is especially large in CanESM5 (maximum change of 1.7 PW), and small in MRI-ESM2-0 (maximum change 0.6 PW). IPSL-CM6A-LR shows the most asymmetric increase between NH and SH, with an average of twice the increase of poleward MSE flux in the SH as in the NH. The average fractional increase in poleward MSE transport in the SH extratropics is 35% in CanESM5, 25% in IPSL-CM6A, and 10% in MRI-ESM2-0.

In each model, there is a part of the high northern latitudes where the poleward MSE transport decreases. This feature is most prominent in MRI-ESM2-0. Hwang et al (2011) argued that models with lesser flux increase into the Arctic were more likely to have stronger polar amplification, due to a diffusive response to high latitude warming causing a diminished energy flux into the Arctic [66]. We return to this Arctic feature later in the paper.

In the NH, the CanESM5 model experiences a large equatorward shift of the maximum MSE flux, of approximately 10 degrees latitude, while the other two models keep the same latitude of maximum northward flux. The maximum in the SH in the CanESM5 model also shifts equatorward by a slightly smaller amount, while the MRI-ESM2-0 and IPSL-CM6A-LR models have a slight poleward shift. The equatorward shifts in maximum.

MSE flux in the CanESM5 indicates especially large increases of MSE flux in the subtropics.

We provide a more detailed explanation for the unique behavior of the CanESM5 model's MSE flux maxima in the following subsections, based on the tropical cloud radiative effect changes.

The northward transport of DSE is plotted in Fig 11C and is the difference between Fig 11A and 11B. The large decrease in poleward transport in the extratropics and increase in poleward transport in the tropics is clear in all models. These oppose the latent energy transport, and thus create a smaller change in MSE transport than in either DSE or latent energy flux individually. Opposition of the latent energy transport by DSE transport occurs at nearly every latitude in each model, and the changes are plotted together in Fig 12A to facilitate comparison. The most prominent exception is in the subtropics (especially visible in the CanESM5 model), where the poleward flux of both the DSE and latent energy increases in both hemispheres.

The CanESM5 model has a particularly large decrease in southward DSE transport in the SH extratropics, where it decreases by over 50% in some places. In all models, the poleward DSE flux decreases particularly strongly in the regions between 35 and 60 degrees. The resulting DSE flux exhibits a poleward shift in the maximum extratropical flux, or the establishment of a new local maximum at high latitudes.

We next consider the compensation percentage, defined as

$$C = \frac{-\Delta F}{latent} \Delta F_{DSE} * 100\%.$$

The compensation percentage C represents the effectiveness of the DSE transport in compensating for the increased latent energy transport, with 100% meaning there is no change in the MSE flux. Compensation percentages within the tropics are larger than 100%, reflecting the fact that the DSE transport increases faster than the latent energy transport. In the Northern Hemisphere between 40 and 60 degrees, compensation percentages are around 75% for each model. In the Southern Hemisphere, percentages are much lower: 65% in MRI-ESM2-0, and 50% in IPSL-CM6A-LR and CanESM5.

How is the compensation percentage in the CanESM5 model in the SH so small, despite the large change in DSE flux? Examining the moisture flux change, one can see that the poleward latent energy transport increases by up to 3 PW, a number that is larger than the poleward transport of DSE in the pre-Industrial period. Thus 100% compensation is impossible within the SH midlatitudes, assuming the DSE transport remains poleward. The picture that emerges

is of a SH storm track in which the latent energy transport increases substantially, working off of large humidity gradients (Figs 3 and 4) despite decreases in DSE transport, driven by some combination of weaker temperature gradients and weaker eddies.

We examine these factors later in the paper.

b. Ocean heat transport. The ocean component of the anomalous northward energy transport is plotted in Fig 12B. This is calculated by integrating the anomalous surface flux after subtracting out the global mean, so includes the effect of both changes in ocean heat transport and differential storage. Since no model is in energy balance by 2300, the differential ocean heat storage is non-negligible. When heat storage is occurring more at the higher latitudes, e.g., in the Southern Ocean, there is an anomalous equatorward energy transport in this metric.

In all three models, the ocean component opposes the MSE transport change. The change in ocean transport is especially close to being equal and opposite to the MSE transport change in the MRI-ESM2-0 model on a latitude-by-latitude basis, while in the CanESM5 model, the ocean transport averages around half of the poleward MSE transport change. The anomalous cross-equatorial transport is strongly negative in the MRI-ESM2-0 model, with a value of -0.5 PW, and is approximately half this value in other two models.

An examination of the anomalous northward transport of energy in the Atlantic Ocean, plotted in the pre-Industrial and warmed climate in Fig 11D, shows that the cross-equatorial anomalies in Fig 12B are primarily due to reductions in strength of the AMOC. In Fig 11D, the x-axis only goes as far south as 30˚ S, due to the end of the ocean basin. CanESM5 only outputs data on ocean heat transport to the year 2180, so in that model we use an average of years 2156 to 2180 to represent the warmed period. In all models, the pre-Industrial ocean circulation transports a large amount of heat northward across the equator, with a similar value of 0.55–0.6 PW, while north of the equator there is substantial model spread in the poleward ocean heat flux. The MRI-ESM2-0 model has 50% larger flux in the pre-Industrial period than the other two models at 45 N.

Warming causes a large decrease in the northward transport of energy in the Atlantic in all three models. AMOC damping is a result of large buoyancy fluxes that help to inhibit deep overturning circulation [67]. While buoyancy changes are primarily driven by surface fluxes [68], this buoyancy flux can also come in the form of melting sea ice, as melt water can cause abrupt changes in the salinity of surface waters [69, 70]. The MRI-ESM2-0 model has a slightly negative Atlantic cross-equatorial transport in the warmed climate, indicating a complete collapse of the AMOC. The AMOC collapse in MRI-ESM2-0 is consistent with the warming pattern in the intermediate period which shows decreased warming south of Greenland, also called the North Atlantic Warming Hole (NAWH; Fig 2I) [71, 72]. The AMOC collapse is likely also the primary cause of the southward ITCZ shift in the Atlantic identified in Fig 6F–6I as the reduction in oceanic heat transport must be met by an northward transport of MSE, which contributes to the convergence of winds occurring farther south [73, 74]. The slowdown in circulation and the accompanying ocean heat flux decrease can help explain the equatorward shift in the ITCZ shown in each model.

Another consistent feature in the ocean heat flux change in Fig 12 is the decrease in strength of the ocean heat divergence within the equatorial region. The subtropical cells are wind-driven, and along with the decrease in strength of the surface winds throughout the tropics, visible both in the change in zonal winds in Fig 7 and in surface wind change plots as a function of latitude and longitude (not shown), the upwelling and overturning circulation must weaken. In turn, the MSE fluxes increase in each model to compensate for the decrease in ocean heat transport.

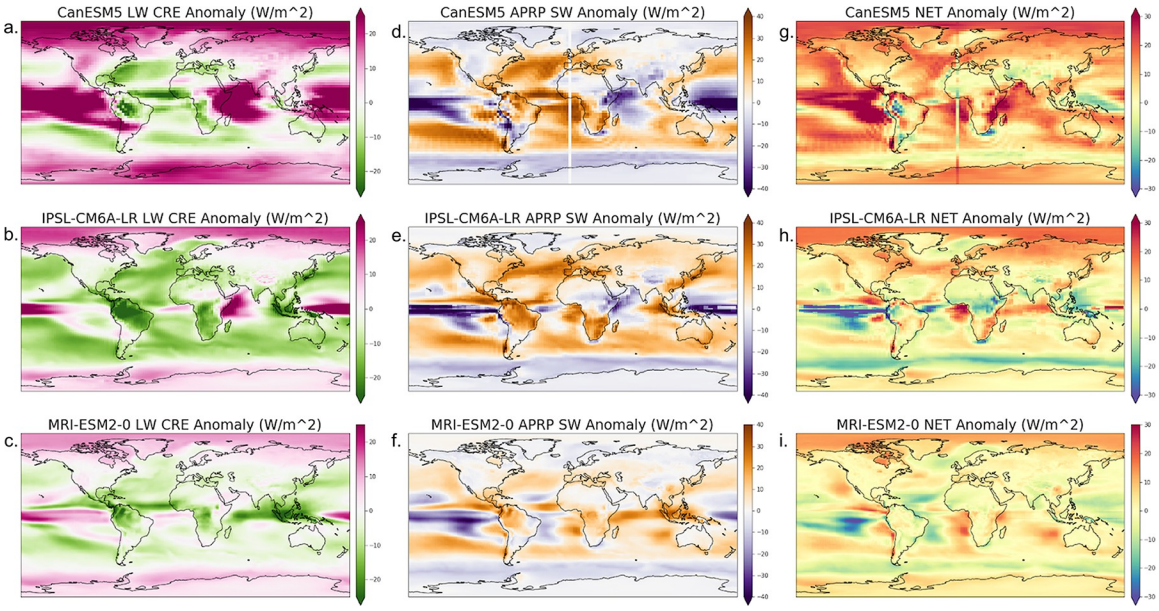

Fig 13. Anomalies in **(A, B, C)** longwave cloud radiative effect, **(D, E, F)** shortwave cloud radiative effect as calculated using APRP, and **(G, H, I)** the sum of the longwave and shortwave cloud radiative effects. These maps were made using the Cartopy Robinson projection (https://scitools.org.uk/cartopy/docs/v0.15/crs/projections.html) which uses data from Natural Earth (https://www.naturalearthdata.com/downloads/110m-physical-vectors/).

https://doi.org/10.1371/journal.pclm.0000343.g013

c. Cloud radiative effect. Clouds can have large contributions to the local and global energy budget, and hence are useful in understanding how energy moves in an extremely warmed climate. The radiative impact of clouds is presented as longwave and shortwave components as well as the net radiative effect in Fig 13. The longwave CRE is simply the difference between the longwave top of atmosphere radiation in clear sky and in all sky conditions. The SW cloud term is found using the Approximate Partial Radiative Perturbation (APRP) method to decompose the shortwave radiation budget into its contributing mechanisms (in this case clouds) [75]. APRP allows us to remove surface effects (such as ice melt) to the shortwave budget from the shortwave cloud effect [76]. The net radiative anomaly is defined as the sum of the longwave CRE and the shortwave APRP cloud effect. Fig 13 shows fields of each metric for cloud radiation as the hot period anomalies from the pre-Industrial average values.

The changes in longwave CRE are quite different among the three models. IPSL-CM6A-LR and MRI-ESM2-0 both experience a global mean negative longwave cloud feedback (meaning the longwave component of CRE acts as a cooling force on global mean radiation). The two models have global mean longwave CREs of -4.9 and -2.6 W/m^2 respectively. The longwave CRE in CanESM5 behaves very differently, and accounts for a total increase in downward longwave radiation. The average longwave CRE anomaly in CanESM5 is 7.0 W/m^2.

Although the global mean values differ, the broad patterns of the changes in longwave CRE are fairly consistent among models, with decreases over regions of marine stratocumulus and strong increases in the tropics. The much larger region of positive longwave CRE anomaly around the equator in CanESM5 is in part due to the large increase in tropical temperature, which increases the depth of deep convective clouds. This is an expected positive feedback to global warming that is well supported by theory, and is on the cusp of being constrained observationally, with rising high clouds currently being observable in the Northern Hemisphere [77–79]. Upward movement of clouds is also associated with increases in tropopause height, visible in both the streamfunction and zonal wind panels (Fig 7). The particularly large

meridional extent of the positive longwave CRE region in CanESM5 suggests an expansion of high clouds throughout the poleward branches of the Hadley circulation. The lack of shortwave cloud cooling in that region points to a potential role of cirrus clouds, which have a large impact on longwave radiation, but are optically thin to solar wavelengths [80], but we are limited by data availability in our ability to understand this feature.

In the shortwave cloud term, there is increased radiation absorbed over much of the subtropics, indicating a reduction of stratocumulus and cumulus clouds, and decreased radiation over parts of the deep tropics and high latitudes. Without cloud fields at varying heights and optical depths, such as is provided by the COSP cloud simulator package [81], we cannot determine what cloud types are contributing to these radiative anomalies.

The differences in the longwave and shortwave cloud radiation result in global net radiative effects of 9.5 W/m^2 for CanESM5, 0.1 W/m^2 for IPSL-CM6A-LR, and MRI-ESM2-0 has a net radiative effect that is balanced to order one thousandth of a W/m^2. Cloud feedbacks are considered the largest source of variability in climate sensitivity [26, 82–84], and Virgin et al. (2021) [85] found that equatorial low cloud and non-low cloud reduction is the primary cause of the high climate sensitivity of CanESM5 compared with the previous generation of that model. The cloud feedbacks are likely an important cause of the particularly large MSE transport increase away from the equator in the CanESM5 model, with MSE transport away from the cloud-induced heating. We return to this feature in the Discussion section.

d. Eddies, lapse rate, and diffusivity. We next examine factors that characterize and affect extratropical eddies to better understand the energy transports presented in Section 3.2. a. The average standard deviation of daily sea-level pressure is used to estimate the eddy intensity in each model. The standard deviation is calculated from daily fields of sea-level pressure, where the seasonal cycle is removed and the pre-Industrial mean is subtracted out. Standard deviation of sea-level pressure calculated in this way indicates the strength of synoptic scale systems and eddies.

The eddy strength is shown in Fig 14 as an average over the last 25 years of the simulation and a percent change compared with pre-Industrial. At the end of the run each model shows a large area of low eddy intensity in the tropics, with high intensity in the midlatitudes and polar regions. There is some positive change in eddy strength in the tropics, but since the pre-Industrial value in those regions is near zero, the large fractional changes are not indicative of large absolute changes. All three models exhibit a weakening of midlatitude surface eddies, each model showing the largest fractional change off the west coast of continents. CanESM5 has the strongest reduction, with many midlatitude regions experiencing a decrease of more than 40%. IPSL-CM6A-LR has fewer regions that decrease by more than 40% and follows a very similar spatial pattern to CanESM5. MRI-ESM2-0 has a much weaker response, especially in the Northern Hemisphere, where very few regions decrease by more than 10%.

One potential cause of the widespread eddy weakening, the lapse rate, is shown in Fig 15. The lapse rate in the hot period and its anomaly from pre-Industrial are plotted, with lapse rate defined as the difference between the temperature at 300 hPa and the surface divided by the difference in geopotential height at 300 hPa and surface. The change in lapse rate in all models is dominated by an increase in the poles, and a decrease in the tropics and subtropics. The lapse rate in the tropics/subtropics decreases due to the decrease in the saturated adiabatic lapse rate at higher temperatures and humidity [86]. Polar amplification of surface warming, on the other hand, is surface-trapped, and causes an increase in the lapse rate [87].

CanESM5 has the largest global-averaged reduction of lapse rate, with a change of -1.24 K/km, then IPSL-CM6A-LR has a change of -1.17 K/km, MRI-ESM2-0 has the smallest net change of -0.66 K/km. Throughout the subtropics and midlatitudes, the models show a decrease in lapse rate (as seen in CMIP3 models in Frierson 2006 [88]), with an especially

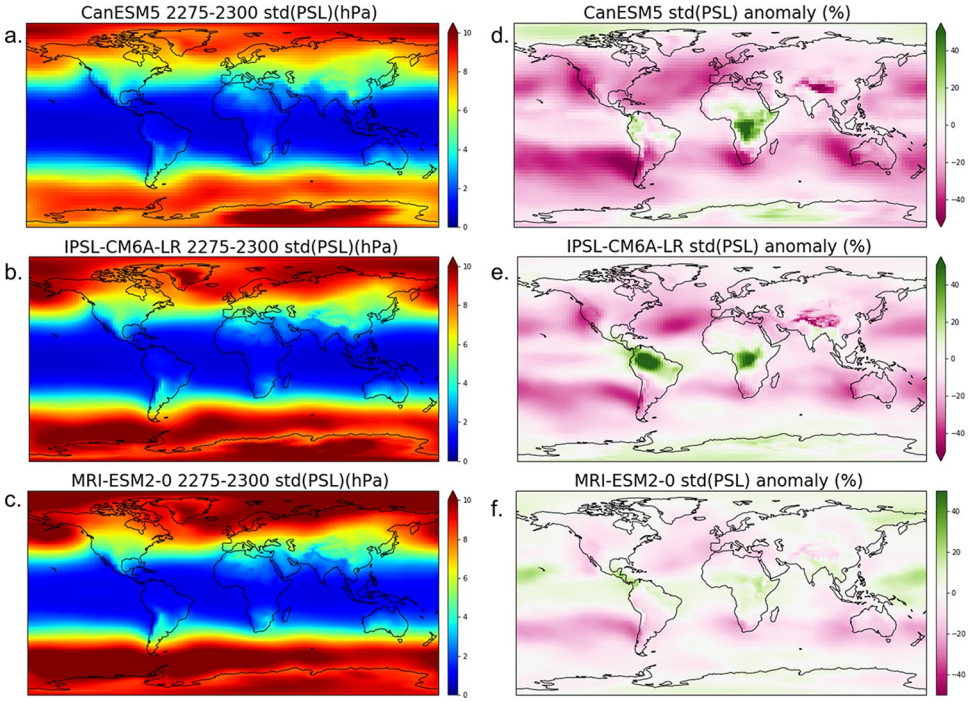

Fig 14. **(A, B, C)** The standard deviation of daily sea level pressure fields (hPa) in the hot period, and **(D, E, F)** the percentage change since pre-Industrial. These maps were made using the Cartopy Robinson projection (https://scitools.org.uk/cartopy/docs/v0.15/crs/projections.html) which uses data from Natural Earth (https://www.naturalearthdata.com/downloads/110m-physical-vectors/).

https://doi.org/10.1371/journal.pclm.0000343.g014

prominent decrease in the CanESM5 model. When the lapse rate decreases, the static stability of the atmosphere increases, so that the eddy kinetic energy is lower, resulting in a decrease in surface eddies [89]. Even though increased moisture content can offset this (and indeed is the original cause of the lapse rate change), the dry static stability is thought to be most relevant because baroclinic instability always has some unsaturated component [90, 91]. It is also possible for the static stability decrease in high latitudes to cause an increase in eddy intensity over the poles.

To investigate how the energy transport is influenced by changes in eddy intensity, we first examine the surface MSE in Fig 16. Since the surface geopotential is the same in both time periods, MSE is equal to

$$MSE = C\Delta T + L\Delta q.$$
$$p \qquad v$$

The MSE increases substantially due to temperature and humidity increases. The increase is largest in the tropics in each model due to the increase in humidity. This results in an increase in the equator-to-pole MSE difference in each model. The increase in MSE gradient likely explains some of the tendency of the flux to increase, but does the weakening of eddies also play a role?

The surface diffusivity, calculated as the vertically integrated MSE flux divided by the meridional gradient in MSE is plotted in Fig 17 to answer this question. Although both the flux and the gradient of MSE increase with warming, the flux increases more in the SH in all models, leading to a decrease in the diffusivity. In the NH, changes in diffusivity are smaller, and not consistent among the three models. The CanESM5 and IPSL-CM6A-LR models each

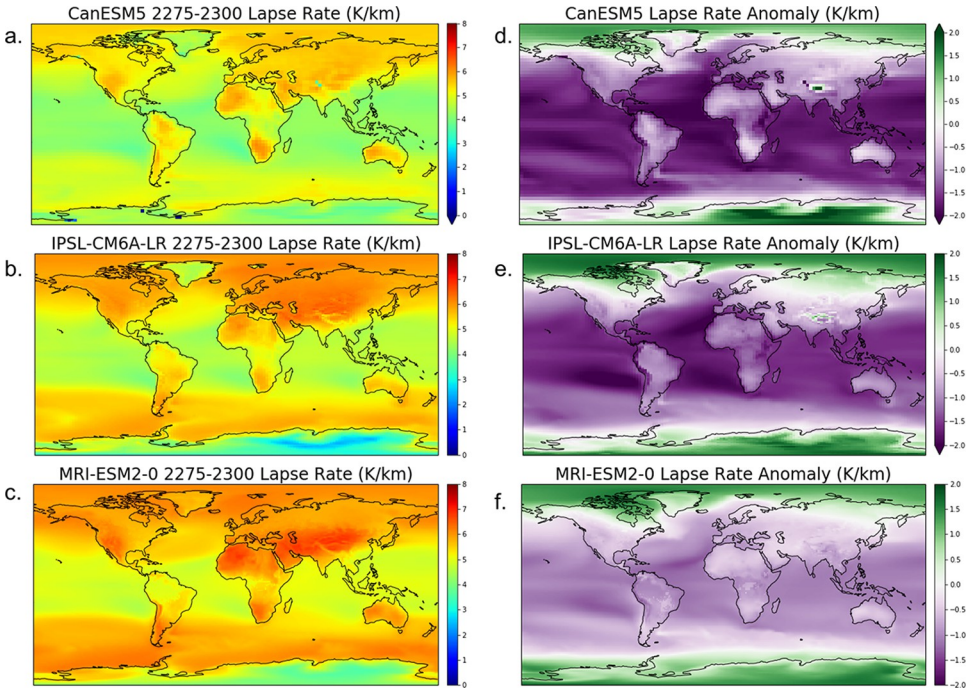

Fig 15. The lapse rate in **(A, B, C)** the hot period, and **(D, E, F)** the change since pre-Industrial, calculated as the difference between the temperature at the surface and 300 hPa, divided by the difference in geopotential height at the same levels. These maps were made using the Cartopy Robinson projection (https://scitools.org.uk/cartopy/docs/v0.15/crs/projections.html) which uses data from Natural Earth (https://www.naturalearthdata.com/downloads/110m-physical-vectors/).

https://doi.org/10.1371/journal.pclm.0000343.g015

show a small decrease in diffusivity when averaged between 25 and 50 degrees North, while MRI-ESM2-0 shows approximately zero change over the same latitude band. This is consistent with the NH eddy changes in the MRI-ESM2-0, which show slight increases in that model as compared to the pre-Industrial level.

4. Discussion and conclusions

Global warming extension scenarios run for several centuries into the future provide a unique laboratory for analysis of climate dynamics in a much warmer world. Despite the lack of certainty about emissions into the distant future and the unlikeliness of this particular pathway, these simulations provide an interesting opportunity for the study of climate changes of the future. Even if these climates are never realized, the large amplitude changes can help with understanding of smaller perturbations. For instance, many of the climate changes that have been observed in the recent past and are expected in the next 50 years are seen in a more extreme manner in these simulations. These include increases in moisture content and transport, poleward shifts of the storm tracks and Hadley cell boundaries, weakening of tropical surface winds, and reductions in the AMOC strength. Global mean temperature increase for these simulations range from 9.3 K to 17.5 K, with moisture content increasing by at least a factor of 1.5 in each model, and with moisture in CanESM5 increasing by more than a factor of 2. While many of the changes we observe are proportional to the global mean temperature, some are not, such as the weakening of the AMOC.

The climate metrics shown can be used together to understand the physical mechanisms responsible for many of the dynamical changes. The massive increases in latent energy

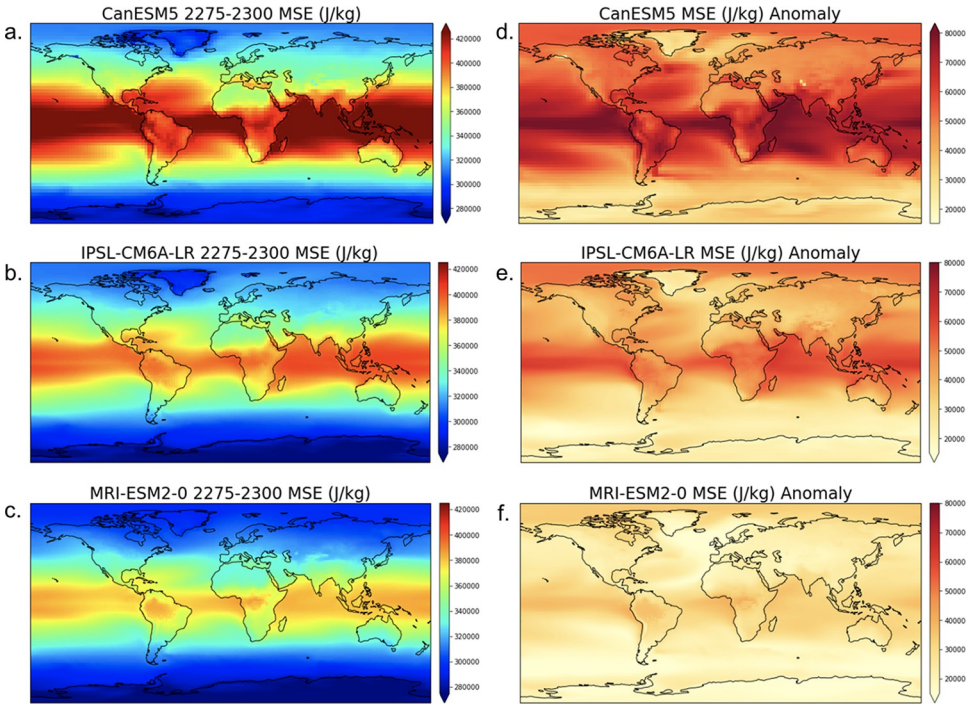

Fig 16. Surface moist static energy (*J/kg*) in **(A, B, C)** the hot period, and **(D, E, F)** the change since pre-Industrial. These maps were made using the Cartopy Robinson projection (https://scitools.org.uk/cartopy/docs/v0.15/crs/projections.html) which uses data from Natural Earth (https://www.naturalearthdata.com/downloads/110m-physical-vectors/).

https://doi.org/10.1371/journal.pclm.0000343.g016

transport are balanced by corresponding decreases in DSE transport, although the compensation is imperfect. The increase in moisture flux is so large in some cases (e.g., the Southern Hemisphere in CanESM5) that perfect compensation is impossible if the DSE transport is to remain poleward. In all models, eddy intensity decreases substantially, likely due to the decreases in lapse rate and decreases in meridional temperature gradient. The eddy intensity decrease is associated with a decrease in MSE diffusivity. Ocean heat transports and cloud radiative effects each influence MSE fluxes and can help understand the difference in energy transports among models.

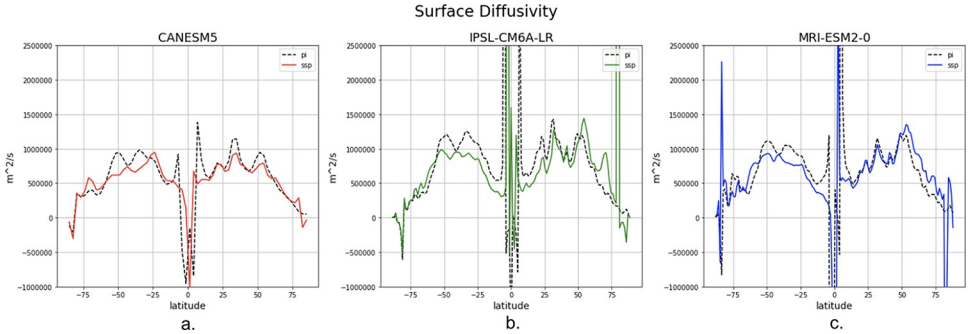

Fig 17. Diffusivity of moist static energy (m^2/s), defined as the vertically integrated MSE flux divided by the surface MSE gradient at each latitude for pre-Industrial (dashed) and the hot period (solid) for **(A)** CanESM5, **(B)** IPSL-CM6A-LR, and **(C)** MRI-ESM2-0.

https://doi.org/10.1371/journal.pclm.0000343.g017

The CanESM5 model has the largest warming, and thus stands out in many of the diagnostics. In terms of energy transports, the difference between CanESM5 and the other two models is most prominent around the equator. The sharp increase in poleward MSE flux in the tropics of CanESM5, described Section 3a, is likely in part due to a transport of MSE away from the large cloud radiative heating in the deep tropics. The Hadley cell transports away any excess of energy input in order to assure that temperature gradients remain flat, and eddies also increase to seamlessly connect the transports. The fact that the Hadley circulation decreases in strength (Figs 7 and 8) means that this increased transport must be due to some combination of increased gross moist stability [27, 92] or increased eddy moisture fluxes.

In addition to the cloud radiative terms, another contributor to the increased MSE flux in the CanESM5 model is the oceanic heat transport (Fig 12). The CanESM5 model experiences the largest decrease in ocean flux divergence in the deep tropics, indicating a decrease in transport by the subtropical cells. This wind-driven circulation declines due to the decrease in wind speed throughout the tropics. In response to the decreased tropical ocean circulation, the Hadley cell and atmospheric eddy energy transports increase. In all models, AMOC declines lead to a reduced southward energy transport across the equator. This is especially strong in the MRI-ESM2-0 model and leads to a southward shift of tropical precipitation.

There is much opportunity for additional climate model experiments similar to the SSP5-8.5ext simulations. Due to the simulation protocol, many aspects of the Earth system that would certainly be changed under such extreme warming are kept fixed. These include the land ice sheets, vegetation types, and the carbon cycle. It would be interesting to examine an intercomparison of fully coupled models that include these processes.

High radiative forcing is one unique aspect of the ECP8.5 and SSP5-8.5 extension simulations, but the extended run length is also important. A recent model intercomparison project aims to understand the century-to-millenium timescale effects of climate change. LongRunMIP is a collection of model simulations that are all at least one thousand years in length, and they each are forced with a constant increase of CO_2 concentrations [93]. Most LongRunMIP simulations have smaller radiative forcing than the ECP8.5 and SSP5-8.5 extension pathways. Studies from LongRunMIP have focused on time-dependent climate sensitivity [94], the spatial structure of feedbacks [95], and estimation of equilibrium climate sensitivity [96]. On centennial to millennial timescales, midlatitude dynamics including the Atlantic basin, dominate global feedback responses [94].

It would also be useful to have a broader range of simulations of warming past 2100. The SSP protocol recommends extension past 2100 of only the extremely high radiative forcing SSP5-8.5ext scenario analyzed here, and the extremely low radiative forcing SSP5-3.4-OSext and SSP1-2.6ext scenarios. Having a range of scenarios with more realistic emissions pathways that are run past 2100 would allow for better quantitative predictions of lasting climate impacts. If there are rapid changes in radiative forcing, or a more sensitive climate than expected, it may be that SSP5-8.5ext simulations will be useful for the understanding of climate impacts in the 22nd and 23rd centuries. Global climate change will not stop in 2100, so it will become increasingly important to understand climate impacts past that date.

Author Contributions

Conceptualization: Dargan M. W. Frierson.

Formal analysis: Alyssa N. Poletti, Dargan M. W. Frierson, Travis Aerenson, Akshaya Nikumbh, Rachel Carroll, William Henshaw.

Funding acquisition: Dargan M. W. Frierson.

Investigation: Dargan M. W. Frierson, Travis Aerenson, Akshaya Nikumbh.

Methodology: Dargan M. W. Frierson.

Project administration: Dargan M. W. Frierson.

Supervision: Dargan M. W. Frierson.

Visualization: Alyssa N. Poletti, Dargan M. W. Frierson, Travis Aerenson, Akshaya Nikumbh, Rachel Carroll, William Henshaw.

Writing – original draft: Alyssa N. Poletti, Dargan M. W. Frierson, Travis Aerenson, Akshaya Nikumbh, Rachel Carroll, William Henshaw.

Writing – review & editing: Alyssa N. Poletti, Dargan M. W. Frierson, Travis Aerenson, Akshaya Nikumbh, Jack Scheff.

References

1. Tripati AK, Roberts CD, and Eagle RA. Coupling of CO2 and Ice Sheet Stability Over Major Climate Transitions of the Last 20 Million Years. Science. 2009; 326(5958), 1394–1397. https://doi.org/10.1126/science.1178296 PMID: 19815724
2. Baker HS, Millar RJ, Karoly DJ, Beyerle U, et al. Higher CO2 Concentrations Increase Extreme Event Risk in a 1.5˚C World. Nature Climate Change. 2018; 8, 604–608. https://doi.org/10.1038/s41558-018-0190-1
3. Clarke B, Otto F, Stuart-Smith R, and Harrington L. Extreme Weather Impacts of Climate Change: An Attribution Perspective. Environmental Research: Climate. 2022; 1(1). https://doi.org/10.1088/2752-5295/ac6e7d
4. Bartusek S, Kornhuber K, and Ting M. 2021 North American Heatwave Amplified by Climate Change-Driven Nonlinear Interactions. Nature Climate Change. 2022; 12, 1143–1150. https://doi.org/10.1038/s41558-022-01520-4
5. Tripathy KP, Mukherjee S, Mishra AK, and Williams AP. Climate Change Will Accelerate the High-end Risk of Compound Drought and Heatwave Events. PNAS. 2023; 120(28). https://doi.org/10.1073/pnas.2219825120 PMID: 37399379
6. Karmalkar AV and Bradley RS. Consequences of Global Warming of 1.5˚C and 2˚C for Regional Temperature and Precipitation Changes in the Contiguous United States. PLOS One. 2017. https://doi.org/10.1371/journal.pone.0168697 PMID: 28076360
7. Haile GG, Tang Q, Hosseini-Moghari S-M, Liu X, et al. Projected Impacts of Climate Change on Drought Patterns Over East Africa. Earth's Future. 2020; 8(7). https://doi.org/10.1029/2020EF001502
8. Archer D. The long thaw: How humans are changing the next 100,000 years of earth's climate. Princeton University Press; 2016.
9. Clark PU, Shakun J, Marcott S, Mix AC, Eby M, Kulp S, et al. Consequences of twenty-first-century policy for multi-millennial climate and sea-level change. Nature Climate Change. 2016; 6: 360–369. https://doi.org/10.1038/nclimate2923
10. Lyon C, Saupe EE, Smith CJ, Hill DJ, Beckerman AP, Stringer et LC, et al. Climate change research and action must look beyond 2100. Global Change Biology. 2021; 28(2): 1–13. https://doi.org/10.1111/gcb.15871 PMID: 34558764
11. Fox-Kemper B, Hewitt HT, Xiao C, Aðalgeirsdóttir G, Drijfhout SS, et al. Ocean, Cryosphere and Sea Level Change. In Climate Change 2021: The Physical Science Basis. Contribution of Working Group I to the Sixth Assessment Report of the Intergovernmental Panel on Climate Change. Cambridge University Press. 2021; 1211–1362. https://doi.org/10.1017/9781009157896.011
12. Lee J-Y, Marotzke J, Bala G, Cao L, et al. Future Global Climate: Scenario-based Projections and Near-term Information. In: Climate Change 2021: The Physical Science Basis. Contribution of Working Group 1 to the Sixth Assessment of the Intergovernmental Panel on Climate Change. Cambridge University Press; 2023.
13. Van Vuuren DP, Edmonds J, Kainuma M, Riahi K, Thomson A, Hibbard K, et al. The representative concentration pathways: an overview. Climatic Change. 2011; 109: 5. https://doi.org/10.1007/s10584-011-0148-z

14. Meinshausen M, Smith SJ, Calvin K, Daniel JS, Kainuma MLT, Lamarque JF, et al. The RCP greenhouse gas concentrations and their extensions from 1765 to 2300. Climatic Change. 2011; 109: 213. https://doi.org/10.1007/s10584-011-0156-z

15. Collins M, Knutti R,Arblaster J, Dufresne JL, Fichefet T, Friedlingstein P, et al. Long-term Climate Change: Projections, Commitments and Irreversibility. In: Climate Change 2013: The Physical Science Basis. Contribution of Working Group I to the Fifth Assessment Report of the Intergovernmental Panel on Climate Change. Cambridge University Press

16. Zickfeld K, Eby M, Weaver AJ, Alexander K, Crespin E, Edwards NR, et al. Long-Term Climate Change Commitment and Reversibility: An EMIC Intercomparison. Journal of Climate. 2013; 26(16), 5782–5809.

17. Jahn A, Holland MM. Implications of Arctic Sea Ice Changes for North Atlantic Deep Convection and the Meridional Overturning Circulation in CCSM4-CMIP5 Simulations. Geophysical Research Letter. 2013; 40(6): 1206–11.

18. Meehl GA, Washington WM, Arblaster JM, Hu A, Teng H, Tebaldi C, et al. Climate System Response to External Forcings and Climate Change Projections in CCSM4. Journal of Climate. 2012; 25(11): 3661–83.

19. Hezel P J, Fichefet I, Massonnet F. Modeled Arctic Sea Ice Evolution through 2300 in CMIP5 Extended RCPs. Cryosphere. 2014; 8(4): 1195–1204.

20. Drijfhout S, Bathiany S, Beaulieu C, Swingedouw D. Catalogue of abrupt shifts in Intergovernmental Panel on Climate Change climate models. PNAS. 2015; 112(42): E5777–E5786. https://doi.org/10.1073/pnas.1511451112 PMID: 26460042

21. Bathiany S, Notz D, Mauritsen T, Raedel G, Brovkin V. On the Potential for Abrupt Arctic Winter Sea Ice Loss. Journal of Climate. 2016; 29(7): 2703–2719. https://doi.org/10.1175/JCLI-D-15-0466.1

22. Hankel C, Tziperman E. The Role of Atmospheric Feedbacks in Abrupt Winter Arctic Sea Ice Loss in Future Warming Scenarios. Journal of Climate. 2001; 34(11): 4435–4447. https://doi.org/10.1175/JCLI-D-20-0558.1

23. Weaver AJ, Sedláček J, Eby M, Alexander K, Crespin E, Fichefet T, et. al. Stability of the Atlantic meridional overturning circulation: A model intercomparison. Geophysical Research Letters. 2012; 39: L20709. https://doi.org/10.1029/2012GL053763

24. O'Neill BC, Tebaldi C, van Vuuren DP, Eyring V, Friedlingstein P, Hurtt G, et al. The Scenario Model Intercomparison Project (ScenarioMIP) for CMIP6. Geoscientific Model Development. 2016; 9(9): 3461–82.

25. Pierrehumbert RT. The hydrologic cycle in deep time climate problems. Nature. 2002; 419: 191–198. https://doi.org/10.1038/nature01088 PMID: 12226673

26. Held IM, Soden BJ. Robust Responses of the Hydrological Cycle to Global Warming. Journal of Climate. 2006; 19(21): 5686–99.

27. Frierson DMW. The Dynamics of Idealized Convection Schemes and Their Effect on the Zonally Averaged Tropical Circulation. Journal of the Atmospheric Sciences 2007; 64: 1959–1976. https://doi.org/10.1175/JAS3935.1

28. Frierson DMW, Held IM, Zurita-Gotor P. A Gray-Radiation Aquaplanet Moist GCM. Part II: Energy Transports in Altered Climates. Journal of the Atmospheric Sciences. 2007; 64(5): 1680–93.

29. Flannery BP. Energy Balance Models Incorporating Transport of Thermal and Latent Energy. Journal of the Atmospheric Sciences. 1984; 41(3): 414–21.

30. Hwang YT, Frierson DMW. Increasing Atmospheric Poleward Energy Transport with Global Warming. Geophysical Research Letters. 2010: 37(24).

31. Roe GH, Feldl N, Armour KC, Hwang YT, Frierson DWM. The Remote Impacts of Climate Feedbacks on Regional Climate Predictability. Nature Geoscience. 2015; 8(2): 135–39.

32. Siler N, Roe GH, Armour KC. Insights into the Zonal-Mean Response of the Hydrologic Cycle to Global Warming from a Diffusive Energy Balance Model. Journal of Climate. 2018; 31(18): 7481–93.

33. Armour KC, Siler N, Donohoe A, Roe GH. Meridional Atmospheric Heat Transport Constrained by Energetics and Mediated by Large-Scale Diffusion. Journal of Climate. 2019; 32(12): 3655–80.

34. Kang SM, Seager R, Frierson DMW, Liu X. Croll Revisited: Why is the northern hemisphere warmer than the southern hemisphere? Climate Dynamics. 2015; 44: 1457–1472. https://doi.org/10.1007/s00382-014-2147-z

35. Lin YJ, Hwang Y, Ceppi P, Gregory JM. Uncertainty in the Evolution of Climate Feedback Traced to the Strength of the Atlantic Meridional Overturning Circulation. Geophysical Research Letters, 2019; 46: 12331–12339. https://doi.org/10.1029/2019GL083084

36. Seidel DJ, Fu Q, Randel WJ, Reichler TJ. Widening of the tropical belt in a changing climate. Nature geoscience. 2008; 1(1):21–4.

37. Staten PW, Reichler T. On the Ratio between Shifts in the Eddy-Driven Jet and the Hadley Cell Edge. Climate Dynamics. 2014; 42(5–6): 1229–42. Stommel H. Thermohaline convection with two stable regimes of flow. Tellus. 1961; 13(2): 224–230.

38. Hu Y, Huang H, Zhou C. Widening and Weakening of the Hadley Circulation under Global Warming. Science Bulletin. 2018; 63(10): 640–44. https://doi.org/10.1016/j.scib.2018.04.020 PMID: 36658884

39. Vecchi GA and Soden BJ. Global warming and the weakening of the tropical circulation. Journal of Climate, 2007; 20, 4316–4340.

40. Meinshausen M, Nicholls Z, Lewis J, Gidden MJ, Vogel E, Freund M, et al. The SSP greenhouse gas concentrations and their extensions to 2500. Geoscientific Model Development. 2019; 13. https://doi.org/10.5194/gmd-2019-222

41. Hausfather Z, Peters GP. Emissions–the 'business as usual' story is misleading. Nature. 2020; 577: 618–620. https://doi.org/10.1038/d41586-020-00177-3 PMID: 31996825

42. Swart NC, Cole JNS, Kharin VV, Lazare M, Scinocca JF, Gillett NP, et al. The Canadian Earth System Model version 5 (CanESM5.0.3). Geoscientific Model Development. 2019; 12(11): 4823–4873. https://doi.org/10.5194/gmd-12-4823-2019

43. Yukimoto S, Kawai H, Koshiro T, Oshima N, Yoshida K, Urakawa S, et al. The meteorological research institute Earth system model version 2.0, MRI-ESM2.0: Description and basic evaluation of the physical component. Journal of the Meteorological Society of Japan. 2019; 97(5), 931–965. https://doi.org/10.2151/jmsj.2019-051

44. Boucher O, Servonnat J, Albright AL, Aumont O, Balkanski Y, Bastrikov V, et al. Presentation and Evaluation of the IPSL-CM6A-LR Climate Model. Journal of Advances in Modeling Earth Systems, 2020; 12 (7): e2019MS002010. https://doi.org/10.1029/2019MS002010

45. Fan X, Duan Q, Shen C, Wu Y, and Xing, C. Global Surface Air Temperatures in CMIP6: Historical Performance and Future Changes. Environmental Research Letters. 2020; 15. https://doi.org/10.1088/1748-9326/abb051

46. Tebaldi C, Debeire K, Eyring V, Fischer E, Fyfe J, Friedlingstein P, et al. Climate model projections from the Scenario Model Intercomparison Project (ScenarioMIP) of CMIP6. Earth System Dynamics Discuss. 2020. https://doi.org/10.5194/esd-2020-68

47. Narsey S, Brown JR, Delage F, Boschat G, Grose M, Colman R, et. al. Storylines of South Pacific Convergence Zone Changes in a Warmer World. Journal of Climate. 2022; 35(20): 2949–2967. https://doi.org/10.1175/JCLI-D-21-0433.1

48. Gregory JM, Ingram WJ, Palmer MA, Jones GS, Stott PA, Thorpe RB, et al. A New Method for Diagnosing Radiative Forcing and Climate Sensitivity. Geophysical Research Letters. 2004; 31(3). https://doi.org/10.1029/2003GL018747

49. Meehl GA, Senior CA, Eyring V, Flato G, Lamarque JF, Stouffer RJ, et al. Context for Interpreting Equilibrium Climate Sensitivity and Transient Climate Response from the CMIP6 Earth System Models. Science Advances. 2020; 6(26). https://doi.org/10.1126/sciadv.aba1981 PMID: 32637602

50. Washington WM, Meehl GA. High-Latitude Climate Change in a Global Coupled Ocean atmosphere-Sea Ice Model with Increased Atmospheric CO2. Journal of Geophysical Research Atmospheres. 1996; 101(D8): 12795–801. https://doi.org/10.1029/96JD00505

51. Holland MM, Bitz CM. Polar amplification of climate change in coupled models. Climate Dynamics. 2003; 21: 221–232. https://doi.org/10.1007/s00382-003-0332-6

52. Serreze MC, Barrett AP, Stroeve JC, Kindig DN, Holland MM. The Emergence of Surface-Based Arctic Amplification. The Cryosphere. 2009; 3: 11–19.

53. Ono J, Watanabe M, Komuro Y, Tatebe H, Abe M. Enhanced Arctic warming amplification revealed in a low-emission scenario. Communications Earth & Environment. 2022; 3: 27. https://doi.org/10.1038/s43247-022-00354-4

54. Sherwood S and Fu Q. A Drier Future? Science. 2014; 343(6172), 737–739. https://doi.org/10.1126/science.1247620

55. Byrne MP and O'Gorman PA. Understanding Decreases in Land Relative Humidity with Global Warming: Conceptual Model and GCM Simulations. Journal of Climate. 2016; 29(24), 9045–9061. https://doi.org/10.1175/JCLI-D-16-0351.1

56. Byrne MP and O'Gorman PA. Trends in Continental Temperature and Humidity Directly Linked to Ocean Warming. PNAS. 2018; 11(19), 4863–4868. https://doi.org/10.1073/pnas.1722312115 PMID: 29686095

57. Yang W, Seager R, Cane MA, Lyon B. The east African long rains in observations and models. Journal of Climate. 2014; 27; 7185–7202. https://doi.org/10.1175/JCLI-D-13-00447.1

58. Giannini A, Lyon B, Seager S, and Vigaud N. Dynamical and thermodynamic elements of modeled climate change at the east African margin of convection. Geophysical Research Letters. 2018; 45: 992–1000. https://doi.org/10.1002/2017GL075486

59. Hu S, Vallis GK. Meridional structure and future changes of tropopause height and temperature. Quarterly Journal of the Royal Meteorological Society. 2019; 145(723):2698–717.

60. Lu J, Vecchi GA, Reichler T. Expansion of the Hadley cell under global warming, Geophysical Research Letters, 2007; 34(6).

61. Zhou W, Xie SP, Yang D. Enhanced equatorial warming causes deep-tropical contraction and subtropical monsoon shift. Nature Climate Change. 2019; 9: 834–839. https://doi.org/10.1038/s41558-019-0603-9

62. Chemke R, Polvani LM, Deser C. The Effect of Arctic Sea Ice Loss on the Hadley Circulation. Geophysical. Research. Letters. 2019; 46(2): 963–972. https://doi.org/10.1029/2018GL081110

63. Grise KM, Davis SM, Simpson IR, Waugh DW, Fu Q, Allen RJ, et al. Recent tropical expansion: Natural variability or forced response? Journal of Climate. 2019; 32: 1551–1571. https://doi.org/10.1175/JCLI-D-18-0444.1

64. Watt-Meyer O, Frierson DMW, Fu Q. Hemispheric Asymmetry of Tropical Expansion Under CO2 Forcing. Geophysical Research Letters. 2019; 46(15): 9231–9240. https://doi.org/10.1029/2019GL083695

65. Barnes EA, Hartmann DL. Detection of Rossby wave breaking and its response to shifts of the midlatitude jet with climate change. Journal of Geophysical Research Atmospheres. 2012; 117(D9). https://doi.org/10.1029/2012JD017469

66. Hwang YT, Frierson DMW, Kay JE. Coupling between Arctic feedbacks and changes in poleward energy transport. Geophysical Research Letter. 2011; 38: L17704, https://doi.org/10.1029/2011GL048546

67. Putrasahan DA, Lohmann K, von Storch JS, Jungclaus JH, Gutjahr O, Haak H. Surface flux drivers for the slowdown of the Atlantic meridional overturning circulation in a high-resolution global coupled climate model. Journal of Advances in Modeling Earth Systems. 2019; 11(5):1349–63.

68. Kostov Y, Johnson HL, Marshall DP. AMOC sensitivity to surface buoyancy fluxes: the role of air-sea feedback mechanisms. Climate Dynamics. 2019; 53: 4521–4537. https://doi.org/10.1007/s00382-019-04802-4

69. Weijer W, Maltrud ME, Hecht MW, Dijkstra HA, Kliphuis MA. Response of the Atlantic Ocean circulation to Greenland ice sheet melting in a strongly eddying ocean model.Geophysical Research Letters. 2012; 39(9). https://doi.org/10.1029/2012GL051611

70. Li H, Fedorov A, Liu W. AMOC Stability and Diverging Response to Arctic Sea Ice Decline in Two Climate Models. Journal of Climate. 2021; 34(13): 5443–5460. https://doi.org/10.1175/JCLI-D-20-0572.1

71. Zhang R, Kang SM., Held. Sensitivity of Climate Change Induced by the Weakening of the Atlantic Meridional Overturning Circulation to Cloud Feedback. Journal of Climate. 2010; 23(2): 378–389. https://doi.org/10.1175/2009JCLI3118.1

72. Jackson LC, Kahana R, Graham T, Ringer MA, Woollings T, Meckinget JV, et al. Global and European climate impacts of a slowdown of the AMOC in a high resolution GCM. Climate Dynamics. 2015; 45: 3299–3316. https://doi.org/10.1007/s00382-015-2540-2

73. Zhang R, Delworth TL. Simulated Tropical Response to a Substantial Weakening of the Atlantic Thermohaline Circulation. Journal of Climate. 2005; 18(12), 1853–1860 https://doi.org/10.1175/JCLI3460.1

74. Yu S, Pritchard MS. A Strong Role for the AMOC in Partitioning Global Energy Transport and Shifting ITCZ Position in Response to Latitudinally Discrete Solar Forcing in CESM1.2. Journal of Climate. 2019; 32(8): 2207–2226. https://doi.org/10.1175/JCLI-D-18-0360.1

75. Taylor KE, Crucifix M, Braconnot P, Hewitt CD, Doutriaux C, Broccoli AJ, et al. Estimating Shortwave Radiative Forcing and Response in Climate Models. Journal of Climate. 2007; 20(11): 2530–43.

76. Zelinka MD, Andrews T, Forster PM, and Taylor KE. Quantifying Components of Aerosol-Cloud-Radiation Interactions in Climate Models. Journal of Geophysical Research: Atmospheres. 2014; 119(12), 7599–7615. https://doi.org/10.1002/2014JD021710

77. Hartmann DL, Larson K. An Important Constraint on Tropical Cloud—Climate Feedback. Geophysical Research Letters. 2002; 29(20): 12-1–12-14.

78. Zelinka MD, Hartmann DL. Why Is Longwave Cloud Feedback Positive? Journal of Geophysical Research Atmospheres. 2010; 115(16).

79. Aerenson T, Marchand R, Chepfer H, Medeiros B. When will MISR detect rising high clouds? Journal of Geophysical Research: Atmospheres. 2022; 127, e2021JD035865. https://doi.org/10.1029/2021JD035865

80. Lynch DK. Cirrus clouds: Their role in climate and global change. Acta Astronautica. 1996; 38(11): 859–863. https://doi.org/10.1016/S0094-5765(96)00098-7

81. Bodas-Salcedo A, Webb MJ, Bony S, Chepfer H, Dufresne JL, Klein SA, et al. COSP: Satellite simulation software for model assessment. Bulletin of the American Meteorological Society. 2011; 92: 1023–1043. https://doi.org/10.1175/2011BAMS2856.1

82. Dufresne JL, Bony S. An Assessment of the Primary Sources of Spread of Global Warming Estimates from Coupled Atmosphere-Ocean Models. Journal of Climate. 2008; 21(19): 5135–44

83. Zelinka MD, Myers TA, McCoy DT, Po-Chedley S, Caldwell PM, Ceppi P, et al. Causes of Higher Climate Sensitivity in CMIP6 Models. Geophysical Research Letters. 2020; 47(1). https://doi.org/10.1029/2019GL085782

84. Sherwood SC, Webb MJ, Annan JD, Armour KC, Forster PM, Hargreaves JC, et al. An Assessment of Earth's Climate Sensitivity Using Multiple Lines of Evidence. Reviews of Geophysics. 2020; 58. https://doi.org/10.1029/2019RG000678 PMID: 33015673

85. Virgin JG, Fletcher CG, Cole JNS, von Salzen K, Mitovski T. Cloud Feedbacks from CanESM2 to CanESM5.0 and their influence on climate sensitivity. Geoscientific Model Development. 2021; 14(9). https://doi.org/10.5194/gmd-14-5355-2021

86. Wetherald RT, Manabe S. Cloud Feedback Processes in a General Circulation Model. Journal of the Atmospheric Sciences. 1988; 45(8), 1397–1415.

87. Pithan F, Mauritsen T. Arctic amplification dominated by temperature feedbacks in contemporary climate models. Nature Geoscience. 2014; 7: 181–184. https://doi.org/10.1038/ngeo2071

88. Frierson DMW. Robust increases in midlatitude static stability in simulations of global warming. Geophysical Research Letters. 2006; 33: L24816, https://doi.org/10.1029/2006GL027504

89. Yuval J, Kaspi Y. Eddy Activity Response to Global Warming–Like Temperature Changes. Journal of Climate. 2020; 33: 1381–1404. https://doi.org/10.1175/JCLI-D-19-0190.1

90. Emanuel KA, Fantini M, Thorpe AJ. Baroclinic instability in an environment of small instability to slantwise moist convection. Part I: Two-dimensional models. Journal of Atmospheric Sciences. 1987; 44: 1559–1573.

91. Zurita-Gotor P. Updraft/Downdraft Constraints for Moist Baroclinic Modes and Their Implications for the Short-Wave Cutoff and Maximum Growth Rate. Journal of the Atmospheric Sciences. 2006; 62(12): 4450–4458. https://doi.org/10.1175/JAS3630.1

92. Neelin JD, Held IM. Modeling Tropical Convergence Based on the Moist Static Energy Budget. Monthly Weather Review. 1987; 115: 3–12. https://doi.org/10.1175/1520-0493(1987)115<0003:MTCBOT>2.0.CO;2

93. Rugenstein M, Bloch-Johnson J, Abe-Ouchi A, Andrews T, Beyerle U, Li C, et al. LongRunMIP: Motivation and Design for a Large Collection of Millennial-Length AOGCM Simulations. Bulletin of the American Meteorological Society. 2019; 100: 2551–2570. https://doi.org/10.1175/BAMS-D-19-0068.1

94. Rugenstein M, Bloch-Johnson J, Gregory J, Andrews T, Mauritsen T, Li C, et al. Equilibrium Climate Sensitivity Estimated by Equilibrating Climate Models. Geophysical Research Letters. 2019; 47(4).

95. Bloch-Johnson J., Rugenstein M., and Abbot DS. Spatial Radiative Feedbacks from Internal Variability Using Multiple Regression. Journal of Climate. 2020; 33(10), 4121–4140. https://doi.org/10.1175/JCLI-D-19-0396.1

96. Dai A, Huang D, Rose BEJ, Zhu J, Tian X. Improved methods for estimating equilibrium climate sensitivity from transient warming simulations. Climate Dynamics. 2020; 54: 4515–4543. https://doi.org/10.1007/s00382-020-05242-1